UNIVERSIDADE FEDERAL DE MINAS GERAIS

Instituto de Ciencias Exatas

Programa de Pós-Graduação em Física

Mirela Rodrigues Valentim

PROPOSAL OF A NOVEL TWO-DIMENSIONAL SEMICONDUCTOR:

A first-principles investigation

Belo Horizonte

2023

Mirela Rodrigues Valentim

PROPOSAL OF A NOVEL TWO-DIMENSIONAL SEMICONDUCTOR:
A first-principles investigation

Dissertação apresentada ao Programa de Pós Graduação em Física da Universidade Federal de Minas Gerais, como requisito parcial à obtenção do título de Mestra em Física.

Orientador: Mário Sérgio de Carvalho Mazzoni

Belo Horizonte

2023

UNIVERSIDADE FEDERAL DE MINAS GERAIS
INSTITUTO DE CIÊNCIAS EXATAS
PROGRAMA DE PÓS-GRADUAÇÃO EM FÍSICA

ATA DE DEFESA DE DISSERTAÇÃO

ATA DA SESSÃO DE ARGUIÇÃO DA 700º DISSERTAÇÃO DO PROGRAMA DE PÓS-GRADUAÇÃO EM FÍSICA, DEFENDIDA POR MIRELA RODRIGUES VALENTIM, orientada pelo professor Mário Sérgio Carvalho Mazzoni, para obtenção do grau de **MESTRE EM FÍSICA**. Às 10 horas de vinte e um de julho de 2023, reuniu-se a Comissão Examinadora, composta pelos professores **Mário Sérgio Carvalho Mazzoni** (Orientador - Departamento de Física/UFMG), **Ângelo Malachias de Souza** (Departamento de Física/UFMG) e **Ronaldo Júnio Campos Batista** (Departamento de Física/UFOP) para dar cumprimento ao Artigo 37 do Regimento Geral da UFMG, submetendo a bacharel **MIRELA RODRIGUES VALENTIM** à arguição de seu trabalho de dissertação, que recebeu o título de **"Proposal of a novel two-dimensional semiconductor: a first-principles investigation"**. A candidata fez uma exposição oral de seu trabalho durante aproximadamente 50 minutos. Após esta, os membros da comissão prosseguiram com a sua arguição e apresentaram seus pareceres individuais sobre o trabalho, concluindo pela aprovação da candidata.

Belo Horizonte, 21 de julho de 2023.

Prof. Mário Sérgio Carvalho Mazzoni
Orientador da estudante
Departamento de Física/UFMG

Prof. Ângelo Malachias de Souza
Departamento de Física/UFMG

Prof. Ronaldo Júnio Campos Batista
Departamento de Física/UFOP

Candidata: Mirela Rodrigues Valentim

Referência: Processo nº 23072.245428/2023-36

SEI nº 2494600

Dedico esta dissertação a meus pais, Rodrigo e Luciene.
Sem vocês, nada disso seria possível.

Agradecimentos

Tive o privilégio de conhecer, trabalhar e conviver com várias pessoas excepcionais ao longo da minha vida e formação. Todas foram importantes para eu chegar até aqui, e gostaria de aproveitar a oportunidade para agradecê-las.

Primeiramente, agradeço enormemente aos meus pais, Rodrigo e Luciene, pelo apoio e amor incondicional que recebi em toda minha vida. Obrigada por sempre acreditarem em mim, muito mais do que eu mesma. Ao meu irmão Mateus, por me ensinar sobre bondade, e aos meus familiares, pelo carinho e presença.

Ao Gabriel, pelo companheirismo, compreensão, paciência e também por colaborar tanto com esta dissertação, sempre lendo, opinando e, mais importante, acrescentando um maravilhoso senso de design a tudo.

Ao meu orientador, Mário Mazzoni, pelos ensinamentos ao longo desses mais de quatro anos em que trabalhamos juntos. Ao pessoal do grupo de pesquisa em estrutura eletrônica da UFMG, que sempre foram solícitos e disponíveis quando precisei de ajuda.

Ao pessoal do laboratório de nanoscopia UHV, por me acolherem tão bem como agregada, por me incluírem nos rolês pessoais e científicos do lab, pelas resenhas e também por muitas discussões sobre física. Aprendi muito com vocês!

Aos meus amigos do CEFET, presentes até hoje na minha vida e companheiros de formação. Às minhas amigas do ensino fundamental, que estiveram presentes em todas as etapas da minha vida. Um agradecimento especial à Allanys, Mariana e Taissa, que são as melhores amigas que alguém poderia ter, e todos os dias me sinto sortuda por tê-las ao meu lado.

Aos meus amigos da UFMG, da graduação e da pós, especialmente ao Nícolas, que foi a primeira pessoa que conheci na física e acabou virando uma amizade que dura até hoje. Também agradeço a todos que tiveram alguma contribuição a esta dissertação, seja opinando sobre o texto, ajudando com ideias ou só ouvindo minhas intermináveis reclamações.

Ao pessoal do colegiado de pós-graduação em física. Aprendi muito nas reuniões que tivemos e foi um grande prazer ter contato com vocês. Consegui ver como o ambiente de trabalho no ensino superior também pode ser leve e descontraído. Um agradecimento especial às meninas da secretaria, que fazem tudo funcionar.

Aos meus professores de física no ensino médio, Gustavo e Rodolfo, os verdadeiros responsáveis por eu estar aqui hoje. Pessoas que me introduziram a essa ciência que busquei a minha vida toda, e o fizeram com tanto carinho e dedicação que logo no primeiro ano já decidi que era o que queria fazer da vida. E estou fazendo. Obrigada por terem

feito meus olhos brilharem tanto!

Aos professores que tive ao longo da graduação e mestrado, nas disciplinas, iniciações científicas e estudo orientado. Não poderia deixar de mandar um agradecimento especial ao Paulo Sérgio, que, além de ter sido meu professor em três disciplinas da graduação, me deu uma força inestimável neste período final do mestrado.

Por fim, mas não menos importante, às agências de fomento CNPq, CAPES e Fapemig, e ao INCT, pelo auxílio financeiro que recebi ao longo da minha formação.

Resumo

A exploração e investigação de materiais bidimensionais (2D) ganharam significativa atenção ao longo dos últimos anos, impulsionado principalmente pelo surgimento do grafeno, um composto de propriedades únicas e com inúmeras aplicações. TMDs, MXenes, nitreto de boro hexagonal, siliceno e fosforeno podem ser mencionados como exemplos de materiais 2D em destaque no momento. Neste trabalho, propomos e caracterizamos um novo material bidimensional com composição química $B_2N_2O_2$, que pode ser visto como uma camada de nitreto de boro oxidada. Empregando uma combinação de técnicas teóricas e computacionais baseadas na Teoria do Funcional da Densidade, previmos várias geometrias de baixa energia e avaliamos suas propriedades. Cálculos realizados utilizando o USPEX, um software para previsão de estrutura cristalina, mostram que a oxidação leva a uma reestruturação substancial. Nas configurações mais estáveis, descobriu-se que os compostos de menor energia resultaram em *slabs* com átomos de nitrogênio arranjados em zigue-zague e ligados a átomos de boro que, por sua vez, encontram-se ligados aos oxigênios. Investigamos sua estabilidade energética, térmica e dinâmica através de cálculos de energia de formação, dispersão de fônons e simulações de dinâmica molecular, a partir dos quais atestamos a notável estabilidade desses materiais. A fim de determinar suas propriedades eletrônicas, realizamos cálculos de estrutura de bandas e mobilidade para um mecanismo mediado por fônons. Enquanto o primeiro revelou que o composto é um semicondutor de gap largo com bandas de bordas parabólicas, o último, realizado seguindo a abordagem do potencial de deformação, indicou grandes valores de mobilidade de elétrons e buracos. Atribuímos esse resultado à existência de canais eletrônicos formados pelas ligações em zigue-zague dos átomos de nitrogênio, que definem as bordas das bandas de condução e de valência. Adicionalmente, propomos um potencial mecanismo de síntese para o material a partir da combinação da funcionalização dos oxigênios juntamente à aplicação de pressão. Por fim, demonstramos que os resultados obtidos neste estudo podem ser estendidos a uma ampla família de compostos bidimensionais, que podem ser investigados em trabalhos futuros.

Palavras-chave: materiais bidimensionais; semicondutores; DFT.

Abstract

The exploration and investigation of two-dimensional (2D) materials have earned significant attention in recent years, primarily driven by the emergence of graphene, a compound of unique properties that allows for numerous applications. TMDs, MXenes, hexagonal boron nitride, silicene and phosphorene can be mentioned as examples of trending 2D materials. In this work, we propose and characterize a novel two-dimensional material with chemical composition $B_2N_2O_2$, which can be regarded as an oxidized boron nitride layer. Employing a combination of theoretical and computational techniques based on Density Functional Theory, we predict a number of low-energy geometries and assess their properties. Calculations performed with USPEX, a software for crystal structure prediction, show that the oxidation leads to a substantial restructuring. In the most stable configurations, the resulting lowest-energy compounds were found to be slabs featuring zigzag arrays of nitrogen atoms bonded to boron atoms which, in turn, are bridged by oxygen. We investigate their energetic, thermal and dynamic stability through formation energy, phonon dispersion calculations and molecular dynamics simulations, from which we found that the structures are remarkably stable. To determine their electronic properties, we carried out band structure and mobility calculations for a phonon-mediated mechanism. The former revealed that the compound is a wide band-gap semiconductor with parabolic band edges, and the latter, performed within the deformation potential approach, indicated large electron and hole mobilities. We ascribe these result to the existence of electronic channels formed by the zigzag array of nitrogen bonds, which define the edges of both conduction and valence bands. Additionally, we propose a potential synthesis mechanism for the compound based on oxygen functionalization and application of pressure. Lastly, we demonstrate that the results obtained in this study can be extended to a broader family of two-dimensional compounds, that can be investigated in future works.

Keywords: two-dimensional materials; semiconductors; DFT.

Contents

Chapter 1

Introduction

The continuous quest for new materials has played an important role in driving technological advancements, particularly in the realm of electronic devices. Two-dimensional (2D) materials, for instance, are a fascinating class of compounds that has captured significant attention over the last few years. Indeed, the reduction of the dimensionality gives rise to unique properties and opens up a wide range of applications, many of which are related to overcoming issues imposed by three-dimensional (3D) materials. One example is the thickness constraints of conventionally used silicon-based semiconductors in transistors, that can be overcome by employing 2D materials [1]. Furthermore, the possibility to manipulate and create layered compounds, such as 2D heterostructures, provides additional versatility. Moreover, 2D materials exhibit enhanced surface areas compared to 3D materials, leading to an increase in their physical and chemical reactivity [2].

The exploration of 2D materials can be traced back to graphene, a compound renowned for its unique properties, such as high conductibility, high carrier mobility, resistance and flexibility. It displays applications in various fields, including medicine, environmental science and electronics [3, 4, 5]. In fact, the success of graphene has ignited an interest in exploring and unraveling two-dimensional structures, some of which are discussed in the subsequent paragraph.

The direct analogs to graphene are the honeycomb structures, such as boron nitride (hBN) and silicene. However, these compounds exhibit distinct properties. While graphene is a conductor, hBN behaves as an insulator. Silicene, although having a similar electronic structure to graphene, is not found in a free standing configuration, and the substrate is expected to have important effects on its properties [6]. In addition to graphene and its analogues, Transition Metal Dichalcogenides (TMDs) have gained attention as a promising family of 2D semiconducting structures. They are characterized by the composition MX_2, being M a transition metal and X an element from group 16 of the periodic table. TMDs, along with their heterostructures, find applications in transistors, solar cells and photodetectors [7]. Other notable 2D materials include MXenes, transition metal oxides and one-element structures such as phosphorene and antimonene. They cover a wide range of distinct properties, with a particular emphasis on semiconducting

materials, that are being widely studied and employed, specially in electronic devices.

Wide-bandgap (WBG) semiconductors, in particular, constitute another important class of materials in the field of applied physics [8, 9, 10]. Gallium nitride (GaN), silicon carbide (SiC), gallium oxide (Ga_2O_2) and zinc oxide (ZnO) are examples of WBG compounds. In fact, they have long been investigated due to potential applications involving operations at high temperatures, high voltages and high frequencies, which are increasingly demanded in various fields such as renewable energy, electronics and transportation [11]. A relatively recent trend is the quest for two-dimensional WBG compounds [12], as they combine the distinct properties of both types of materials in the same system.

In this respect, it is well known that oxidation is an important process in 2D systems: almost all 2D materials are susceptible to oxygen functionalization at room temperature [13]. Indeed, while oxidation may be a major problem in realizing potential applications, especially concerning those related to performance in nanoelectronics, it may also pave the way for desired structural transformations, providing modulation of electronic properties and ultimately leading to new forms of 2D materials. For instance, few-layer antimonene may undergo an oxidation driven 2D-1D transition, resulting in well-ordered and stable nanoribbons [14]. Other materials, such as few-layer graphene, may be transformed into graphene oxide and find important applications [15].

In spite of being more resistant to oxidation than graphene, hexagonal boron nitride is also prone to interactions with oxidative species [16]. A question then arises on the possibility to achieve 2D-WBG materials via reactions of known structures with oxygen. May the transformations induced by oxygen incorporation lead to materials with superior properties relative to the parent structures, such as higher mobilities, greater thermal stability and/or modulation of gap energies?

In the present work, we address the above question by considering the particular case of an oxidized boron nitride layer in a stoichiometry $B_2N_2O_2$. We make use of theoretical and computational methods to propose and investigate low-energy geometries for this compound, and therefore assess their properties. Remarkably, our findings revealed that the best geometries resulted to be stable high mobility WBG semiconductors. We assign these results to the geometry of the nitrogen bonds, which formed one-dimensional zigzag arrays. Furthermore, a novel family of structures based on our results is suggested.

After a brief introduction to the context in which this work takes place, the organization of the thesis is detailed. Chapter 2 presents a description of the theory behind the computational approach and implementations used for this work. Density Functional Theory, the *ab initio* formulation and necessary approximations for computational calculations are briefly discussed. Chapter 3 introduces the problem that we investigate in this work and corresponding general objectives. Details of the search for the best

crystalline structures to describe a boron nitride oxide are presented and the results are discussed. At the end of the chapter, three geometries are selected for further analysis. Chapter 4 consists of the theoretical characterization of the selected structures. Structural and electronic aspects of the geometries are evaluated from results obtained using first principles calculations of DFT-based programs SIESTA and VASP. A discussion is made about how the geometry of the nitrogen bonds interfere in the electronic structure and carrier mobilities of the compounds. Lastly, in chapter 5, we present the conclusions of the work, gathering the central points discussed along the thesis.

Chapter 2
Methodology

A new way to understand physics was established in the twentieth century. While classical mechanics could not describe systems in the atomic scale, quantum mechanics has shown itself as a very accurate theory when it comes to describing those systems, its results and effects. The equation that describes the behavior of a quantum system composed of electrons and nuclei is the so-called Schrödinger equation:

$$H\psi(\vec{r}, \vec{R}) = E\psi(\vec{r}, \vec{R}) \tag{2.1}$$

In this equation, ψ denotes the wavefunction and it depends on the electron coordinates $\vec{r}$ and on the nuclei coordinates $\vec{R}$. That is a very important variable in quantum mechanics since it contains all the information about the system [17], being an analogue to the position in classical mechanics. The energy eigenvalue is denoted as E, and H denotes the Hamiltonian. The latter consists of an operator that represents the total energy of the system, namely the sum of all kinetic and potential energies of all particles. In a many-electron system, the Hamiltonian in atomic units can be written as [18]:

$$H = -\sum_{i=1}^{N} \frac{1}{2}\nabla_i^2 - \sum_{A=1}^{M} \frac{1}{2M_A}\nabla_A^2 - \sum_{i=1}^{N}\sum_{A=1}^{M} \frac{Z_A}{|\vec{r_i} - \vec{R_A}|}$$
$$+ \sum_{i=1}^{N}\sum_{j>i}^{N} \frac{1}{|\vec{r_i} - \vec{r_j}|} + \sum_{A=1}^{M}\sum_{B>A}^{M} \frac{Z_A Z_B}{|\vec{R_A} - \vec{R_B}|} \tag{2.2}$$

where A and B refer to the nuclei, while i and j refer to the electrons. M_A denotes the mass of nucleus A and Z_A, Z_B denote the atomic number of nuclei A and B. In atomic units, the charge and mass of the electron and Planck's constant are equal to the unity.

The first two terms of equation (2.2) are the electrons and nuclei kinetic energy operators, respectively. The third term is the electron-nucleus potential energy operator, the fourth term is the electron-electron potential energy operator and the last term is the nucleus-nucleus potential energy operator.

2.1 Born-Oppenheimer approximation

One way to simplify the problem of solving the Schrödinger equation for the Hamiltonian given by (2.2) lies on the fact that the protons are much heavier than the electrons (around a thousand times heavier) and their coordinates can be considered to be steady in a classical framework, while the coordinates of the electron are dynamic. That is to say, due to their larger mass, the nuclei move much slower than the electrons in a way that their displacement can be ignored and they can be treated as static point charges. Thus, the dependence of the variables on the nuclei positions is parametric. This is supported by 1927 paper by Born and Oppenheimer [19], in which perturbation theory was used to show that there are no differences between the Hamiltonians with and without considering interactions with the nuclei up to fourth order terms [20]. This work explains why the approximation is valid and gives the name to it: the Born-Oppenheimer approximation.

When applying this approximation, the wavefunctions of the electrons and the nuclei can be treated independently. The final effect on equation (2.2) is that the kinetic energy of the nuclei is neglected, the nucleus-nucleus potential energy is constant and the Hamiltonian becomes:

$$H_{elec} = -\sum_{i=1}^{N} \frac{1}{2} \nabla_i^2 - \sum_{i=1}^{N} \sum_{A=1}^{M} \frac{Z_A}{|\vec{r_i} - \vec{R_A}|} + \sum_{i=1}^{N} \sum_{j>i}^{N} \frac{1}{|\vec{r_i} - \vec{r_j}|} \tag{2.3}$$

which is called the electronic Hamiltonian. The Schrödinger equation for this Hamiltonian now involves an electronic wavefunction, which depends explicitly on the electron coordinates and parametrically on the nucleus coordinates, $\Phi_{elec} = \Phi_{elec}(\{\vec{r_i}\}, \{\vec{R_A}\})$. The electronic energy only depends parametrically on the nuclear coordinates, $\varepsilon_{elec} = \varepsilon_{elec}(\{R_A\})$. The Schrödinger equation for the electronic Hamiltonian is then written as:

$$H_{elec} \; \Phi_{elec}(\vec{r_i}, \vec{R_A}) = \varepsilon_{elec}(R_A) \; \Phi_{elec}(\vec{r_i}, \vec{R_A}) \tag{2.4}$$

The total energy of the many-electron system relative to the total Hamiltonian with fixed nuclei is the sum of the electronic energy with the constant nucleus-nucleus repulsion term:

$$\varepsilon_{tot} = \varepsilon_{elec} + \sum_{A=1}^{M} \sum_{B>A}^{M} \frac{Z_A Z_B}{|\vec{R_A} - \vec{R_B}|} \tag{2.5}$$

The nuclear problem can also be considered in a similar way by writing its own Hamiltonian and energies. That is the great advantage presented by the Born-Oppenheimer approximation: it decouples the motion of electrons and nuclei. However, our focus is on the electron problem and from now on the *elec* subscript is omitted.

2.2 Molecular orbital theory and LCAO

There are many different ways to describe the electronic structure of molecular systems. One of the most succeeded ones is through molecular orbital theory (MOT), an important method developed by Robert Mulliken et al. that has given him the 1966 Nobel Prize in Chemistry [21]. Orbitals are nothing but a mathematical function that describes the electronic structure and wave-like behavior of electrons - namely, wavefunctions. The idea behind it comes from Bohr's work on atomic wavefunctions and molecular orbitals can be seen as an extension to atomic orbitals, therefore consisting of a method to describe the electronic structure of electrons in molecules. The way of treating the problem proposed by MOT consists of not assigning each molecular orbital to a specific atom or chemical bond, but to consider molecular orbitals as being spread all over the molecule.

Before writing the molecular wavefunctions (alternatively, molecular orbitals), an important feature of molecular systems must be considered. Since only the electronic problem is being considered and knowing that electrons are fermions, the molecular wavefunctions must follow Pauli exclusion principle. This principle states that the wavefunction must change its sign in case of an exchange of two identical particles, requiring an antisymmetric wavefunction to describe them. At first, the spin feature of electrons is put together with its orbital feature. Being $\psi_i(x_m, y_m, z_m)$ the molecular orbital of the electron m in the state i, the molecular spin-orbital is written as follows:

$$\psi_i(q_m) = \psi_i(x_m, y_m, z_m, S_m) = \psi_i(x_m, y_m, z_m)\xi(S_m)$$

where $\xi(S_m)$ defines the spin of the electron by the following function:

$$\xi(S_m) = \begin{cases} \alpha(m) & \uparrow \\ \beta(m) & \downarrow \end{cases}$$

A convenient way of writing antisymmetric functions is through Slater determinants. For a N-electron system, with each electron occupying a state in the set $\{\psi_1, \psi_2, ..., \psi_N\}$, the molecular ground state is therefore written as:

$$|\Psi_0\rangle = \frac{1}{\sqrt{N!}} \begin{vmatrix} \psi_1(1) & \psi_2(1) & ... & \psi_N(1) \\ \psi_1(2) & \psi_2(2) & ... & \psi_N(2) \\ \vdots & \vdots & \ddots & \vdots \\ \psi_1(N) & \psi_2(N) & ... & \psi_N(N) \end{vmatrix} \tag{2.6}$$

where $\frac{1}{\sqrt{N!}}$ is a normalization factor and each ψ denotes a molecular spin-orbital.

When also considering all the infinite excited states $|\Psi_a^r\rangle$, a complete basis set is obtained. Hence, the total wavefunction can be linearly spanned by this set of states.

One way to write molecular orbitals of periodic systems from previously known variables is by using linear combination of atomic orbitals (LCAO). This technique must be combined with Bloch's theorem [22], which states that solutions of the Schrödinger equation on crystals for a given state j, where the potential takes the form $V(\vec{r}) = V(\vec{r} + \vec{R})$, $\vec{R}$ being a lattice vector, satisfy:

$$\psi_j(\vec{r} + \vec{R}) = e^{i\vec{k}\cdot\vec{R}}\psi_j(\vec{r}) \tag{2.7}$$

or, similarly:

$$\psi_j(\vec{r}) = e^{i\vec{k}\cdot\vec{R}}\psi_j(\vec{r} - \vec{R}) \tag{2.8}$$

In order to find an expansion for the wavefunction, a basis set must be previously defined. The idea is to start from atomic orbitals ϕ_j (centered on an atom in the primitive cell) in an expression that also follows Bloch's theorem. A basis set that agrees with the given conditions can be built similarly to equation (2.8), straightforwardly following Bloch's theorem by the inclusion of the exponential factor:

$$\Phi_j(\vec{k}, \vec{r}) = \frac{1}{\sqrt{N!}} \sum_{\vec{R}}^{N} e^{i\vec{k}\cdot\vec{R}}\phi_j(\vec{r} - \vec{R}) \tag{2.9}$$

where $\frac{1}{\sqrt{N!}}$ is a normalization factor and Φ_j are the so-called Bloch functions. Thus, the crystal orbitals ψ_j are written as a linear combination of the Bloch functions:

$$\psi_j(\vec{k}, \vec{r}) = \sum_{j'} C_{j,j'}\Phi_{j'}(\vec{k}, \vec{R}) \tag{2.10}$$

The coefficients $C_{j,j'}$ can be calculated by applying the variational principle to minimize the energy, which leads to a secular equation.

2.3 Density functional theory

The study of lots of interesting systems, specially the ones that realistically replicate macroscopic structures, involves solving the Schrödinger Equation for hundreds or even thousands of electrons. On the other hand, it is well known that obtaining analytical solutions of the Schrödinger Equation is virtually impossible when the problem involves many interacting electrons, since electron-electron interaction terms and kinetic energy make the problem extremely complicated.

For one to obtain the physical properties of the system, it is necessary to diagonalize the Hamiltonian to have the eigenvalues and eigenvectors and, then, calculate the mean value of the operator related to the property in question. However, the dimension of the Hamiltonian increases factorially with the increase of the number of particles, so even powerful computers cannot overcome the operational difficulty and it should be again pointed out that real nanomaterials contains hundreds of interacting particles.

A classical treatment cannot deliver important properties about these materials. Hence it is important to treat these systems using quantum theory and that is why DFT (Density Functional Theory) had accomplished such success among the scientific community: it makes the problem treatable.

2.3.1 Hohenberg-Kohn theorems

The DFT formalism is characterized by using the electronic density as basic variable instead of the wave function, the electronic density being essentially the probability to find the electron in an infinitesimal volume element around a certain point in space. The advantage of this change of variables is that the former has $3N$ variables in a N-electron system, while the latter is a scalar field of only three spatial variables. Surprisingly, all the physical properties of the system can be calculated from the electronic density of the ground state. That is to say, for one to obtain all the information about the system, it is only necessary to know its ground state. This alternative approach was first proposed by Hohenberg and Kohn in their 1964 paper [23], in which two utterly important theorems were introduced.

For a system of interacting particles in an external potential V_{ext} such as the nuclear potential described in (2.3) in the Born-Oppenheimer approximation, the Hamiltonian can be rewritten as:

$$
\begin{aligned}
H &= T + V_{ei} + V_{ee} \\
&= -\sum_{i=1}^{N} \frac{1}{2}\nabla_i^2 + V_{ext} + \sum_{i=1}^{N}\sum_{j>i}^{N} \frac{1}{|\vec{r_i} - \vec{r_j}|}.
\end{aligned}
\tag{2.11}
$$

The terms T, V_{ei} and V_{ee} respectively denotes the kinetic energy, the potential energy between electrons and ions and the potential energy between interacting electrons. Since this Hamiltonian describes a system of interacting electrons, the first Hohenberg-Kohn (HK) theorem applies to it:

Theorem I: For a system of interacting electrons under the influence of an external potential $V_{ext}(\vec{r})$, the potential $V_{ext}(\vec{r})$ is uniquely determined by the ground-state electronic density $n_0(\vec{r})$, up to a trivial additive constant.

Proof: Assume two distinct external potentials $V_{ext}(\vec{r})$ and $V'_{ext}(\vec{r})$ that are different by more than an additive constant. This means that the Hamiltonians of both systems are also different, as well as their ground state wavefunctions $\Psi_0(\vec{r})$ and $\Psi'_0(\vec{r})$. Now assume that both systems lead to the same ground state electronic density $n_0(\vec{r})$. The lowest

possible energy for the system is given by its ground state energy, which is, by definition:

$$E_0 = \langle \Psi_0 | H | \Psi_0 \rangle$$

$$E_0' = \langle \Psi_0' | H' | \Psi_0' \rangle$$

Hence, given that the system is nondegenerate, the energy relative to the trial state $\Psi_0'(\vec{r})$ in the system governed by H must necessarily be greater than E_0:

$$E_0 < \langle \Psi_0' | H | \Psi_0' \rangle = \langle \Psi_0' | H - H' + H' | \Psi_0' \rangle = E_0' + \langle \Psi_0' | H - H' | \Psi_0' \rangle$$
$$= E_0' + \langle \Psi_0' | V_{ext} - V_{ext}' | \Psi_0' \rangle$$

Since V_{ext} and V_{ext}' differ by more than an additive constant, the last term can be rewritten as:

$$\langle \Psi_0' | V_{ext} - V_{ext}' | \Psi_0' \rangle = \int d\vec{r} \left[V_{ext}(\vec{r}) - V_{ext}'(\vec{r}) \right] n_0(\vec{r})$$

The result is the following inequality:

$$E_0 < E_0' + \int d\vec{r} \left[V_{ext}(\vec{r}) - V_{ext}'(\vec{r}) \right] n_0(\vec{r}) \tag{2.12}$$

The same scheme can be done assuming the state $\Psi_0(\vec{r})$ in the system governed by H'. Analogously, its energy must be greater than E_0', leading to the inequality:

$$E_0' < E_0 + \int d\vec{r} \left[V_{ext}'(\vec{r}) - V_{ext}(\vec{r}) \right] n_0(\vec{r}) \tag{2.13}$$

Adding equation (2.12) to equation (2.13), the contradiction becomes evident:

$$E_0' + E_0 < E_0 + E_0' \tag{2.14}$$

Therefore, two different external potentials cannot lead to the same electronic density. That is to say, the ground state electronic density uniquely determines $V_{ext}(\vec{r})$ up to an additive constant. ∎

An important corollary of this theorem is that the knowledge of the ground state electronic density implies the knowledge of all properties of the system, since the wavefunction can be uniquely determined by the Hamiltonian and therefore used to calculate any desired property.

The first Hohenberg-Kohn theorem can be summarized by the following scheme:

$$
\begin{array}{ccc}
V_{ext}(\vec{r}) & \Longleftarrow & n_0(\vec{r}) \\
\Downarrow & & \Uparrow \\
\Psi_i(\vec{r}) & \Longrightarrow & \Psi_0(\vec{r})
\end{array}
$$

The ground state electronic density uniquely determines the external potential through first HK theorem. $V_{ext}(\vec{r})$ determines the Hamiltonian of the system, therefore making possible to solve the Schrödinger equation and obtain all possible states $\Psi_i(\vec{r})$, being the ground state $\Psi_0(\vec{r})$ one among them. All ground state properties can then be calculated, such as $n_0(\vec{r})$, completing the scheme.

For the second theorem, an observation about the Hamiltonian (2.11) must be first stated. The terms T and V_{ee} are universal, i.e., they do not change according to the system. The only term that specifies changes in the system is V_{ei}. Hence, a universal function for the energy can be defined:

$$F[n] = \langle \Psi_0[n]| \, T + V_{ee} \, |\Psi_0[n]\rangle \tag{2.15}$$

and the specific term of the system in the Hamiltonian can be written as:

$$V_{ei} = \int d\vec{r} \, V_{ext}(\vec{r}) n(\vec{r}) \tag{2.16}$$

Knowing both terms, the second Hohenberg-Kohn theorem is stated:

Theorem II: For a given external potential, the energy functional $E[n]$ is defined as:

$$E[n] = F[n] + \int d\vec{r} \, n(\vec{r}) V_{ext}(\vec{r}) \tag{2.17}$$

The electronic density that minimizes $E[n]$ is the ground state electronic density $n_0(\vec{r})$ and the corresponding value of this functional is the ground state energy E_0.

Proof: Recalling HK first theorem, the ground state energy E_0 associated with the ground state wavefunction Ψ_0 corresponds to the ground state electronic density n_0. Now taking a trial electronic density n':

$$E[n'] = \langle \Psi_0[n']| \, H \, |\Psi_0[n']\rangle \; \geq \; E_0 = \langle \Psi_0[n_0]| \, H \, |\Psi_0[n_0]\rangle \tag{2.18}$$

Hence, the minimum value of the energy functional occurs at $n' = n_0$. ∎

In summary, the second HK theorem sets a very useful property: if one knows the form of the energy functional or at least have a glimpse of it, in order to find the ground state it is only necessary to find the lowest possible energy by varying the density.

Even though it was only discussed the non-degenerate version of the HK theorems, it is possible to extend the theorem to degenerate ground states. It is also possible to formulate the theorem in terms of other variables, such as spin-densities for spin-polarized systems.

2.3.2 Kohn-Sham formulation

The Kohn-Sham (KS) formulation proposes a scheme to solve the problem stated by the Hohenberg-Kohn theorems, namely, finding the ground state density. The idea is to consider an auxiliary system consisting of non-interacting electrons and look for the external potential that generates the same electronic density as the original system in the ground state [24]. Even though this formulation offers an excellent route to solve the problem, it also presents a problem: the equations must be solved self-consistently. That is, although the problem is being solved in the auxiliary simpler system, its external effective potential $V_s(\vec{r})$ depends on the electronic density. In the following paragraphs, we focus on finding an expression for this potential.

Considering the system comprised of non-interacting particles, the energy functional can be written as:

$$E_s[n] = T_s[n] + V_s[n], \tag{2.19}$$

where $T_s[n]$ is the kinetic energy and $V_s[n]$ is the ionic potential given in (2.16), with $V_s(\vec{r})$ as the external potential. The subscript s is used to denote the non-interacting system.

Now considering the system of interacting particles, the energy functional is given by equation (2.17), but it can be cleverly rewritten as:

$$E[n] = F[n] + \int n(\vec{r}) V_{ext}(\vec{r}) d\vec{r},$$

$$E[n] = T_s[n] + E_{xc}[n] + \frac{1}{2} \iint \frac{n(\vec{r}) n(\vec{r'})}{|\vec{r} - \vec{r'}|} d\vec{r} d\vec{r'} + \int n(\vec{r}) V_{ext}(\vec{r}) d\vec{r}, \tag{2.20}$$

where the exchange-correlation functional E_{xc} is defined:

$$E_{xc}[n] = F[n] - T_s[n] - \frac{1}{2} \iint \frac{n(\vec{r}) n(\vec{r'})}{|\vec{r} - \vec{r'}|} d\vec{r} d\vec{r'}. \tag{2.21}$$

The $E_{xc}[n]$ term comprises all the unknown information about the system. The idea is to subsequently use approximations to this term.

From the second HK theorem, we recall that the ground-state corresponds to the lowest possible value of the energy functional. Taking the variation of (2.19) and (2.20) with respect to $n(\vec{r})$ and evaluating them in the ground-state electronic density (which is, by construction, the same for both systems):

$$\frac{\delta E[n]}{\delta n(\vec{r})} = \frac{\delta T_s[n]}{\delta n(\vec{r})} + \frac{\delta E_{xc}[n]}{\delta n(\vec{r})} + \int \frac{n(\vec{r'})}{|\vec{r} - \vec{r'}|} d\vec{r'} + V_{ext}(\vec{r}) = 0, \tag{2.22}$$

$$\frac{\delta E_s[n]}{\delta n(\vec{r})} = \frac{\delta T_s[n]}{\delta n(\vec{r})} + V_s(\vec{r}) = 0. \tag{2.23}$$

After comparing and manipulating the equations, an expression for the effective potential is found to be:

$$V_s(\vec{r}) = V_{ext}(\vec{r}) + V_{xc}(\vec{r}) + V_H(\vec{r}), \tag{2.24}$$

where the exchange-correlation potential $V_{xc}(\vec{r})$ and the Hartree potential are defined:

$$V_{xc}(\vec{r}) = \frac{\delta E_{xc}[n]}{\delta n(\vec{r})}, \tag{2.25}$$

$$V_H(\vec{r}) = \int \frac{n(\vec{r'})}{|\vec{r} - \vec{r'}|} d\vec{r'}. \tag{2.26}$$

One can therefore make a first assumption to the trial density and substitute it in the $V_s[n]$ expression, knowing $V_s(\vec{r})$ from (2.24). Once $V_s[n]$ is known, the Hamiltonian of the non-interacting system can be built, leading to the Kohn-Sham equations:

$$\left[-\frac{\hbar^2}{2m}\nabla^2 + V_{ext} + V_{xc} + V_H \right] \psi_i = \varepsilon_i \psi_i. \tag{2.27}$$

Solving these equations for an initial guess for the density $n(\vec{r})$, a new density is obtained:

$$n(\vec{r}) = \sum_{i=1}^{N} |\psi_i(\vec{r})|^2, \tag{2.28}$$

and the scheme is repeated iteratively until self-consistency is achieved, that is, until the difference between input and output densities falls below a specified convergence threshold. The convergence of the non-interacting electron problem implies the solution of the original interacting system, since they have the same ground-state electronic density.

2.3.3   Hellmann-Feynman theorem

In the previous subsection, we introduced equation (2.20) to describe the energy of our system. Now we turn our attention to the task of calculating forces on ions, which relate to the energy through the equation:

$$\vec{F}(i) = -\vec{\nabla} E(i). \tag{2.29}$$

The Hellmann-Feynman theorem [25] provides a method to calculate forces based on the energy.

Theorem: Taking a Hamiltonian $H(\lambda)$, which depends on a parameter λ, and being $|\psi_\lambda\rangle$ its normalized eigenvectors with eigenvalues $E(\lambda)$:

$$H(\lambda)|\psi_\lambda\rangle = E(\lambda)|\psi_\lambda\rangle. \tag{2.30}$$

The Hellmann-Feynman theorem states that the energy derivative relative to the parameter λ can be written as:

$$\frac{dE(\lambda)}{d\lambda} = \langle\psi_\lambda| \frac{dH(\lambda)}{d\lambda} |\psi_\lambda\rangle. \tag{2.31}$$

The proof of this theorem can be found in reference [26].

Taking the parameter λ as a direction in which the force is applied and recalling equation (2.29), the Hellmann-Feynman theorem express that the forces on ions can be calculated as:

$$\vec{F}(\lambda) = -\frac{\partial E(\lambda)}{\partial \lambda} = -\langle \psi_\lambda | \frac{dH(\lambda)}{d\lambda} | \psi_\lambda \rangle. \tag{2.32}$$

This relation is employed in DFT calculations to assess the forces acting on ions, enabling the optimization of geometries. This type of calculation is known as structural relaxation, which involves iteratively adjusting the positions of the ions in order to find a configuration that, besides minimizing forces on ions, also corresponds to a local minimum of the energy.

2.3.4 Exchange-Correlation functional

As mentioned before, the exchange-correlation functional comprises all the unknown information about the system and it must be treated in an approximate way in order to implement the KS scheme. The simplest but still very useful approach to do this is through the Local-Density Approximation (LDA) [24], one of the first successful approximations to the functional.

In general, $E_{xc}[n]$ is non-local, i.e., its value in $\vec{r}$ depends on the density in all other points $\vec{r'}$ of the space and not only in $\vec{r}$. The idea behind LDA is, as the name suggests, to do a local approximation to the exchange correlation functional, considering that the density of the original system varies smoothly in space so that it can be locally considered the same as that of a uniform electron gas of density $n(\vec{r})$. The exchange-correlation energy in this approximation is then written as:

$$E_{xc}^{LDA}[n] = \int n(\vec{r}) \varepsilon_{xc}(n(\vec{r})) d\vec{r}, \tag{2.33}$$

where $\varepsilon_{xc}(n(\vec{r}))$ is the exchange-correlation energy per electron of a homogeneous electron gas of density $n(\vec{r})$. However, not even $\varepsilon_{xc}(n(\vec{r}))$ can be calculated analytically. The $\varepsilon_{xc}(n)$ term is therefore decomposed into exchange and correlation parts:

$$\varepsilon_{xc}(n) = \varepsilon_x(n) + \varepsilon_c(n). \tag{2.34}$$

Now, the problem resides on finding expressions to $\epsilon_x[n]$ and $\epsilon_c[n]$. The exchange part can be analytically calculated for the homogeneous gas using the Hartree-Fock theory [22]:

$$\varepsilon_x^{HF}(n) = -\frac{3e^2}{4\pi}(3\pi^2 n)^{1/3}. \tag{2.35}$$

The correlation part, on the other hand, is not that straightforward to calculate. However, there are many approximations to this term. An important approach was

proposed by Perdew and Zunger in 1980 [27]. It consists of analytically calculating correlation terms in the limits of low density and high density of an uniform electron system. They are set to a certain medium density later on and forced to be continuous. The correlation energy in the Perdew-Zunger parametrization is finally written as:

$$\varepsilon_c^{unif} = \begin{cases} -0,1423/(1+1,0529 \cdot r_s^{1/2} + 0,3334 \cdot r_s), & r_s \geq 1 \\ -0,0480 + 0,0311 \cdot \ln(r_s) - 0,0116 \cdot r_s + 0,0020 \cdot r_s \ln(r_s), & r_s < 1 \end{cases} \quad (2.36)$$

where r_s is the Wigner-Seitz radius and all the coefficients were calculated using Monte Carlo by Ceperley and Alder [28] for the unpolarized case. However, other methods can be implemented. This approach gives an excellent approximation to the exchange-correlation functional, resulting in very similar values when compared to way more laborious numerical techniques.

Another method comprises a generalization of LDA to spin polarized systems. It is the so called LSDA (Local Spin Density Approximation) and its exchange-correlation energy is written as:

$$E_{xc}^{LSDA}[n] = \int n(\vec{r})\varepsilon_{xc}(n_\uparrow, n_\downarrow)d\vec{r}. \quad (2.37)$$

The calculation of E_{xc}^{LSDA} follows in a similar manner to the LDA case.

Even though LDA consists of a local approximation in which the electron density is assumed to vary smoothly, it results in good predictions for systems in which the density varies quickly in space, such as metallic surfaces. The explanation is that LDA underestimates the exchange energy and overestimates the correlation energy in a way that, at some level, the exchange and correlation errors cancel each other out. Another advantage of LDA is that the result represents the exchange-correlation of a real system, an infinite homogeneous electron gas, so that basic rules such as the sum rules and some constraints are satisfied [29].

As mentioned, LDA treats the exchange-correlation locally as the same of an infinite homogeneous electron gas. This term can be thought of as being the zeroth order term of the expansion of the exchange-correlation energy with respect to variations in density [29]. A more accurate approach to E_{xc} consists of considering first order variations on the density. Thus, changes in density away from the coordinate are also taken into consideration, improving some results. This is the so called Generalized Gradient Approximation (GGA) [30] [31] and it has the following form:

$$E_{xc}^{GGA} = \int f_{xc}(n_\uparrow, n_\downarrow, \nabla n_\uparrow, \nabla n_\downarrow) \, d\vec{r}, \quad (2.38)$$

where f_{xc} is a universal function of the spins up and down and their gradients. While the analogous function for f_{xc} in LDA, ε_{xc}, is well established, the best choice for f_{xc} varies. The most used ones are based on the work of Perdew-Burke-Ernzerhof (PBE) [31],

Becke [32] and Perdew-Wang [33]. The PBE parametrization is specially useful and a more detailed description of it is given in the following paragraphs.

In the PBE model, the GGA correlation part for the uniform density condition is represented in the form:

$$E_c^{GGA} = \int n(\vec{r})[\varepsilon_c^{LDA}(r_s, \zeta) + H(r_s, \zeta, t)]d\vec{r}, \tag{2.39}$$

and each variable is specified as follows:

- $r_s = (3/4\pi n)^{1/3}$ is the local Seitz radius,

- $\zeta = (n_\uparrow + n_\downarrow)/n$ is the relative spin polarization,

- $t = |\nabla n|/2\phi k_s n$ is a dimensionless density gradient,

- $\phi(\zeta) = [(1+\zeta)^{2/3} + (1-\zeta)^{2/3}]/2$ is a spin scaling factor,

- $k_s = \sqrt{4k_F/\pi a_0}$ is the Thomas-Fermi screening wave number,

- $k_F = (3\pi^2 n)^{1/3}$ is the Fermi momentum of a Fermi gas,

- $H = (e^2/a_0)\gamma\phi^3 \ln[1 + \frac{\beta}{\gamma}t^2(\frac{1+At^2}{1+At^2+A^2t^4})]$ is the gradient contribution to the correlation,

- $\beta \simeq 0,066725$ and $\gamma \simeq 0,031091$ are coefficients, and

- $A = \frac{\beta}{\gamma}[\exp(-\varepsilon_c/(\gamma\phi^3 e/a_0)) - 1]^{-1}$, being ε_c the same as that from (2.34).

The exchange part is then constructed:

$$E_x^{GGA} = \int n(\vec{r})\varepsilon_x(n)F_x(s)d\vec{r} \tag{2.40}$$

where $\varepsilon_x(n)$ is the same from (2.34), $F_x(s)$ is given by $F_x(s) = 1 + \kappa - \kappa/(1 + \mu s^2/\kappa)$ and $s = |\nabla n|/2k_F n$. The expression for F_x was also proposed by Becke [32] and there are different values for the coefficients μ and κ calculated by both PBE and Becke.

While LDA gives poor results for some observables such as bond dissociation energy and bulk modulus of solids, GGA calculations provide much better results to these observables. Even though showing great improvement in comparison to LDA, GGA calculations have basically the same computational complexity as LDA [29]. However, one must be aware that there is no guarantee that GGA gives better outcomes compared to LDA in specific systems. In fact, there are some systems in which the LDA approach produces more accurate results than GGA.

There are many other ways of approximating the exchange-correlation functional. One last description is given for a class of approximations called hybrid functionals. It

consists of using the exact exchange part calculated from the Hartree-Fock formalism and the correlation part from other sources. This class was first proposed by Becke in his 1993 paper [34] and the great advantage presented by it is the improved accuracy of molecular properties. These functionals are thereupon widely used among the physics and chemistry community. The implementation is straightforward to existing codes for molecular systems, since Hartree-Fock and DFT are default theories to treat them. However, the calculations for solids may become computationally highly complex. The most remarkable feature of hybrid functionals is the great improvement in calculations of bandgap and excitation energies.

2.4   Pseudopotentials

An important feature of the electronic density of atoms is that not all the electrons have the same weight on chemical bonds. In fact, while valence electrons have a big contribution to these bonds, the electronic density near the nucleus almost do not change according to the chemical environment, since electrons in that region (core electrons) are tightly bound to the nucleus. It is thus possible to split the electrons in two groups: core and valence electrons. To simplify calculations, the Coulomb potential of the original system plus the effect of core electrons can be substituted by a pseudopotential that acts on valence pseudofunctions and accurately mimics its electronic behaviour.

The motivation behind the use of pseudopotentials originally stemmed from the search for an appropriate basis set for expanding the wavefunction. A method using Orthogonalized Plane Waves (OPW) was proposed, which consists of constructing plane-wave basis functions for valence states under the condition that the valence and core states are orthogonal. The valence wavefunction can be expanded in an OPW basis set of valence and core terms:

$$|\Psi_k^v\rangle = |\Phi_k^v\rangle - \sum_c |\Psi_k^c\rangle \langle \Psi_k^c | \Phi_k^v \rangle .$$ (2.41)

Here, the subscripts v and c represents valence and core, respectively, and $|\Phi_k^v\rangle$ represents the smooth part of the valence wavefunction, which we call the pseudofunction. The valence pseudofunction is simple and can be expanded within few plane-wave terms. The second term, however, regards the core region, characterized by rapid spatial variation and numerous nodes, therefore requiring more components in the expansion.

An expression for the valence pseudo-eigenstates can be found considering the Schrödinger equation for each valence and core wavefunction as being described by the same electronic Hamiltonian:

$$H |\Phi_k^v\rangle = E_k^v |\Phi_k^v\rangle ,$$ (2.42)

$$H |\Phi_k^c\rangle = E_k^c |\Phi_k^c\rangle .$$ (2.43)

Substituting equation (2.41) in (2.42) and considering (2.43), the modified expression for the Schrödinger equation of non-interacting electrons is obtained:

$$H' \ket{\Phi_k^v} = E_k^v \ket{\Phi_k^v}, \tag{2.44}$$

where we introduce V^{ps} as the pseudopotential and $\ket{\Phi_k^v}$ as the valence pseudofunctions:

$$H' = -\frac{\nabla^2}{2} + V_{ps}, \tag{2.45}$$

$$V^{ps} = V_s(\vec{r}) + \sum_c (E_k^v - E_k^c) \ket{\Psi_k^c} \bra{\Psi_k^c}. \tag{2.46}$$

While the effective potential $V_s(\vec{r})$ is attractive, the second pseudopotential term $\sum_c (E_k^v - E_k^c) \ket{\Psi_k^c} \bra{\Psi_k^c}$ is repulsive, resulting in a weak pseudopotential that is easier to deal with in *ab initio* calculations. This leads to a problem governed by the modified Hamiltonian H' and a simpler pseudofunction $\ket{\Phi_k^v}$, which can be expanded using a small number plane-wave terms.

To ensure that the modified description captures the essential properties of the original system, it must accurately replicate its scattering properties. Apart from this requirement, there are no strict conditions on the pseudopotential, making them non-unique. Consequently, V^{ps} can be conveniently chosen to be weaker and smoother, which, together with the smooth pseudofunction, generates a faster convergence [26]. Hence, the resulting equation (2.44) represents a generalized eigenvalue problem. This formulation was initially proposed by Phillips and Kleinman [35] in 1959 and Antončík [36] in 1960 and it is the precursor of modern pseudopotential formulations.

There are two main approaches to pseudopotentials: the empirical approach, in which the pseudopotential parameters are fitted to experimental data, and the *ab initio* approach, in which V^{ps} is constructed to reproduce the valence properties calculated by the Schrödinger equation for the atomic case. The latter is the most commonly used approach, and one particularly useful and used form of construction is the Norm-Conserving Pseudopotentials (NCPs). These potentials are known for their remarkable accuracy and transferability, meaning that they perform well in various chemical environments. Hamann, Schluter, and Chiang [37] outlined a set of desirable properties for NCPs in their 1979 paper:

1. Real and pseudo valence eigenvalues should agree for a chosen reference atomic configuration.

2. Real and pseudo atomic wavefunctions should agree beyond a chosen core radius R_c.

3. The charge inside the sphere for a radius beyond the core radius should agree for both real and pseudo systems. That is, the integrals of the charge from 0 to r for each valence state in the real and pseudo systems agree for $r > R_c$ (norm conservation).

4. The logarithmic derivatives of the real and pseudo wavefunction and their first energy derivatives should agree for $r > R_c$.

Property 3 together with the fact that both pseudo and real systems are spherically symmetric guarantees that the electric potentials agree outside R_c through Gauss's law. On the other hand, property 4 states that the pseudopotential dependence on the energy will be of second order and thus can be ignored with minimum error to the scattering properties of the real system. These two properties ensure important points to make the NCPs more transferable, indicating that they can be built in a simple atomic environment and then be applied to more complex ones, such as crystals and molecules, which involves chemical bonds.

A significant contribution to the development of *ab initio* norm-conserving pseudo-potentials was made by Troullier and Martins (TM) [38]. The TM pseudopotentials follow all the NCPs properties mentioned earlier and they are specifically designed to be smooth without any nodes in the valence pseudo wavefunctions. Recalling the spherical symmetry of the system, the starting point for the construction is self-consistently solving the radial Kohn-Sham equation for a reference system consisting of a real atomic configuration (also known as *all-electron*):

$$\left(-\frac{1}{2}\frac{d^2}{dr^2} + \frac{l(l+1)}{2r^2} + V_s(\rho, r) \right) rR_l(r) = \varepsilon_l rR_l(r), \tag{2.47}$$

where $R_l(r)$ is the radial all-electron wavefunction, $V_s[\rho, r]$ is the self-consistent one-electron potential given as the sum of the ionic, Hartree and exchange-correlation potentials. The idea is to substitute the all-electron wavefunction inside the core radius to a smooth pseudofunction, which is taken to be:

$$R_l(r) = r^l e^{p(r)} \quad , \quad r \le R_c, \tag{2.48}$$

while keeping the wavefunction unchanged outside R_c. Here, $p(r)$ is the polynomial $p(r) = c_0 + c_2 r^2 + c_4 r^4 + c_6 r^6 + c_8 r^8 + c_{10} r^{10} + c_{12} r^{12}$ and its coefficients can be determined from the NCPs properties.

Figure 1 displays an illustrative comparison between pseudo and *ab initio* all-electron valence wavefunctions and potentials for molybdenum.

2.5 Computational implementations

In the present study, we conducted *ab initio* DFT calculations using two computational implementations: SIESTA [39] and VASP [40]. These implementations are characterized by their respective methodologies, which are described in detail in the following paragraphs.
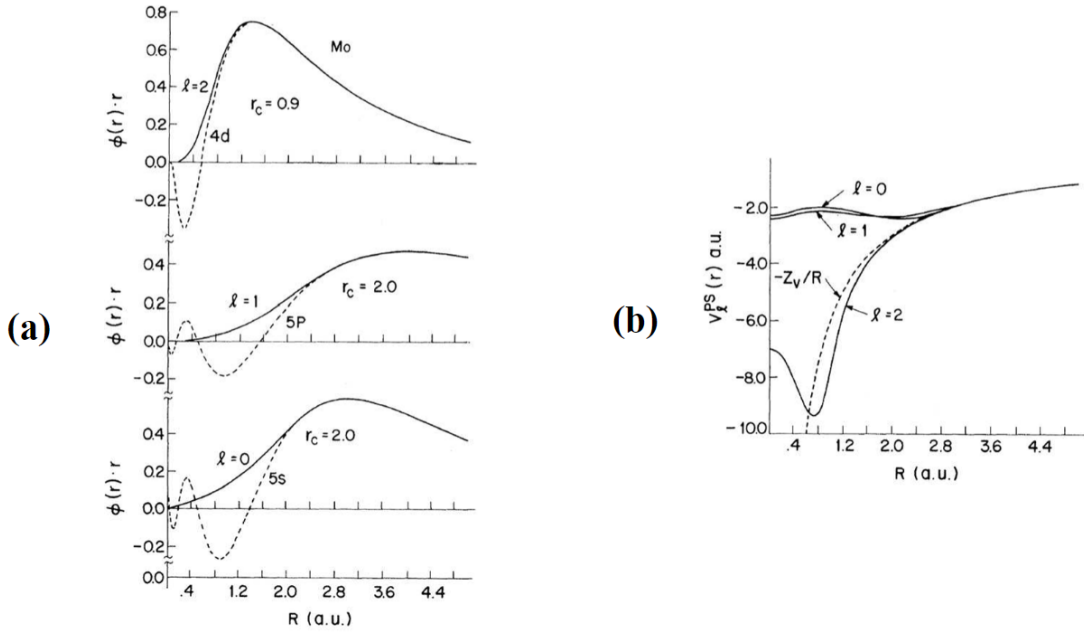
Figure 1 – Comparison of all-electron and pseudo **(a)** radial wavefuncions and **(b)** potentials for $l = 0,\ 1,\ 2$ for Mo. Figure replicated from reference [37].

SIESTA, an acronym for *Spanish Initiative for Electronic Simulations with Thousands of Atoms*, is both a method and its implementation to perform electronic structure calculations and molecular dynamics simulations. Its key feature is the employment of a numerical localized basis set of pseudo atomic orbitals, implemented through the LCAO approach. This is done by defining a cutoff radius r_c, and the atomic orbitals of the basis set outside this radius are set to zero. It is important to mention that r_c is set to be beyond the region at which chemical bonds take place, therefore not compromising the results. The electronic density and the Hamiltonian are also rewritten to be localized and this process leads to many simplifications. Some parameters become dependent only on the interatomic distances, allowing for precalculation and storage of these results in tables, that are further used by the program. It also operates making use of pseudopotentials, which are available for a wide range of chemical elements. The greatest advantage of the SIESTA method is its linear scaling behaviour with the number of atoms in the construction of the Hamiltonian, enabling calculations with both few and many atoms in the primitive cell. However, SIESTA is limited to using the LDA and GGA approximations for the exchange-correlation functional.

The second implementation is VASP (*Vienna ab-initio Simulation Package*), a computer program for matter modeling from first principles. Conversely to SIESTA, VASP offers support for hybrid functionals, which provide improved accuracy for band gap calculations compared to LDA and GGA. It also employs pseudopotentials using norm-conserving, ultrasoft or PAW parametrizations. However, VASP expresses key quantities such as the electronic density, the local potential and the pseudopotential itself

in plane-wave basis sets. To accelerate the calculations, methods involving the application of Broyden and Pulay schemes to iteratively diagonalize large matrices are apllied, leading to a scaling behaviour of N^2 for systems containing up to 1000 atoms.

The combination of these two unique computational tools allowed for the exploration of their advantages, facilitating the investigation of various electronic and structural properties of the studied systems.

2.6   Molecular dynamics simulations

In conditions of fixed volume, number of particles and temperature, the average kinetic energy can be regarded as a measure of the temperature. This is a direct consequence of the average process in the ensemble consistent with these constraints, the canonical ensemble, which is behind the energy equipartition theorem. Also, this result suggests an approach to achieve the target temperature in a molecular dynamics (MD) simulation: by scaling the particle velocities in each time step, it is possible to control the average kinetic energy and, consequently, the temperature. This approach is extensively employed in several MD schemes and, among these, one of the most employed is the so-called Berendsen thermostat [41].

However, there is a fundamental issue. To calculate averages of physical observables at a specific temperature, the system must have its trajectories generated in the canonical ensemble, which means that the statistical knowledge of the system must come from the specific form of the partition function of this ensemble. This is not accomplished by simply scaling the particle velocities.

Shuichi Nosé [42] devised an ingenious scheme to fulfill this requirement. In his approach, a fictitious degree of freedom is associated to the scaling variable. This implies the definition of virtual variables, which represent an extended system formed by the actual system coupled to a heat bath. The crucial point is that the extended Hamiltonian incorporates kinetic and potential energy contributions responsible for the dynamics of the scaling variable. In particular, the form of the potential energy is chosen so as to make the partition function of the real variables coincide with the partition function of a canonical ensemble at the target temperature.

The method may be described by representing the physical system with *real variables* (q', p', t') and introducing the additional degree of freedom s, which acts as an external system. The extended system is built by using s as a scaling variable, which

relates the real variables (q', p', t') to the virtual variables (q, p, t):

$$q'_i = q_i,$$
$$p'_i = p_i/s,$$
$$dt' = dt/s.$$

The next step is the introduction of the Hamiltonian of the extended system, postulated as:

$$H = \sum_i \frac{p_i^2}{2m_i s^2} + \Phi(\vec{q}) + \frac{p_s^2}{2Q} + gkT\ln(s), \qquad (2.49)$$

in which $\Phi(\vec{q})$ is the potential energy of the physical system, Q is the inertial (mass) parameter of the fictitious degree of freedom in units of $[energy] \cdot [time]^2$, g is a parameter which we shall relate to the number of degrees of freedom of the system, T is the target temperature, $gkT\ln(s)$ is the fictitious energy potential and p_s is the conjugate momentum of s.

The idea now is to recognize that energy is conserved in the extended system, so it produces trajectories in the microcanonical ensemble. This means that, in the virtual coordinates (unprimed quantities), the partition function is:

$$Z = \int dp_s \int ds \int d\vec{p} \int d\vec{q}\, \delta \left[H_0(\vec{p}/s, \vec{q}) + \frac{p_s^2}{2Q} + gkT\ln(s) - E \right]. \qquad (2.50)$$

By changing coordinates from unprimed to primed variables, and performing the integration in the s variable, it turns out straightforwardly that the partition function can be cast in the following form if g is chosen to be $3N + 1$, with N being the number of particles:

$$Z = C \int d\vec{p'} \int d\vec{q'} e^{-H_0(p', q')/kT}. \qquad (2.51)$$

This equation represents the canonical ensemble. The integration is supported by the fact that the argument of the δ function has only one zero [42], which we represent as s_0, therefore allowing for the use of the following property for the delta function: $\delta[f(s)] = \delta(s - s_0)/f'(s_0)$. This representation leads to a split of the integral in uncoupled terms, resulting in the characteristic exponential from the canonical ensemble, as given in equation (2.51).

The parameter Q must be chosen at the beginning of the simulation. If Q is too large, the coupling to the bath is weak and there will be large temperature fluctuations. If Q is too small, the "s-motion" will be characterized by high frequencies, which will produce high-frequency oscillations in the temperature. An estimate of a good value for Q is given by:

$$Q = \frac{2gkT}{\omega_c^2}, \qquad (2.52)$$

in which ω_c is a characteristic phase frequency of the real system.

Chapter 3

Structure prediction: The case of a boron nitride oxide

One (1D) and two-dimensional (2D) materials have been broadly searched and studied over the last few decades, motivated by the discovery of carbon structures with astonishing properties such as nanotubes and nanosheets. These nanostructures showed that reduction of the dimension can give rise to interesting properties. In particular, the quest for new 2D materials became popular since graphene was obtained and characterized in 2004 [43], an important work that leaded Andre Geim and Konstantin Novoselov to a Nobel Prize in Physics in 2010. The emergence of novel two-dimensional materials, such as TMDs, MXenes and phosphorene, was strongly influenced by this context.

An interesting property of B-N bonds is that they comprise the same number of electrons as C-C bonds, directly originating BN counterparts for various carbon materials. Hence, a BN analogue to graphene turned out quick- and straightforwardly: a BN nanosheet characterization were reported within one year of the graphene breakthrough [44]. Although leading to similar structures, B-N bonds induce a site-symmetry breaking relative to C-C bonds, therefore giving rise to distinct properties. One example is two-dimensional hexagonal boron nitride (2D-hBN or just hBN), that is an insulator of outstanding stability, whereas graphene is an exceptional conductor. However, recent studies show that, despite being more resistant than graphene, hBN may also be susceptible to oxidation, specially under high temperatures [45].

Oxidation is indeed a process that can change not only the structure of a material, but also its properties. Graphene oxide, for instance, has been extensively investigated due to its promising applications in electronic, optics, chemistry, energy storage and biology [46]. This leads to the following question: can interesting crystalline materials also arise from the oxidation of hBN?

There are reports in the literature on the oxidation of hBN under high temperatures [47], with suggestions of potential applications [48]. However, not much is known about the product of this reaction. Even though an amorphous phase has been reported [49], it is still an open issue if crystalline phases can be generated from this process.

The present work is motivated by this context and, in a first moment, consists of a theoretical search for stable crystalline structures that can be regarded as boron nitride oxides in the specific stoichiometry $B_2N_2O_2$. In a second step, we conducted a systematic characterization of the proposed structures, including electronic and stability aspects. Interestingly, we found that the lowest-energy structures present 1D arrays of nitrogen atoms arranged in zigzag patterns, which, to a large extent, define the low-energy properties of the compounds. We show that the compounds may achieve large electron and hole mobilities due to electronic channels furnished by the zigzag nitrogen lines. The structures are also remarkably stable, as probed by phonon dispersions and molecular dynamics simulations.

3.1 Search for the oxidized hBN structure

To recap, the first motivation for the study was to try to find possible structures arising from the oxidation of hBN by O_2. The idea was to search for stable low-energy 2D structures having the fixed stoichiometry $B_2N_2O_2$. In order to evaluate if a certain structure is likely to exist in nature, energetic aspects and stability properties must be considered. That is because, even though it is widely known that the energy must be located at a local minimum, this does not guarantee that the structure is stable. Therefore, stability parameters such as phonon dispersion and elastic modulus must also be evaluated.

To get some feeling on why these parameters are important, it must be recalled that they are related to the way the structure respond to changes in its geometry. The changes can be caused by, for example, natural vibrations of the lattice. Thus, if the structure is located at a energy minimum but does not have good stability indicatives, it probably will not resist to natural vibrations of the lattice, therefore evolving to a different geometry. This dynamics can be considered from the mentioned stability parameters.

After these considerations, the work can be summarized as a search for structures that are located at local energy minima but, at the same time, show stability properties befitting its existence in nature. However, there are infinite ways to arrange the atoms in the lattice and hence predicting the crystal structure would involve evaluating the energy and stability parameters of infinite structures. By good luck, that is not necessary.

3.1.1 Crystal structure prediction

The crystalline structure of a solid is a crucial piece of information that enables the calculation of many of its properties. In practical terms, predicting the structure of a crystal consists in finding the global and local minima on the free energy hypersurface of the considered chemical composition. Each point on this surface represents the energy of a specific crystal configuration (atomic coordinates and lattice parameters). The local

minimum points consist of metastable structures, and those with the lowest energies are more likely to exist in nature.

However, this surfaces lies on a highly multidimensional configuration space. More specifically, the free energy is a function of 3N+3 degrees of freedom, where N represents the number of atoms, and finding local minima of multidimensional functions can be rather complicated. Point-by-point exploration of the surface is not feasible. The good news is that there is no need to explore the whole surface, but only some promising and physically consistent regions. One way to locate them is through experimental data, that provide valuable information about the structure. While it is possible to determine the crystal structure from experimental data, doing so from a theoretical framework alone is challenging and requires numerous considerations.

Currently, there are two approaches to predict the structure of a crystal. Both are only possible because they take account of physical properties of the system in order to apply constraints and reduce the regions of searching. The first consists in starting already in a good region of the configuration space and looking for deeper local minima nearby. Some examples are metadynamics, simulated annealing and basin hopping. While this approach works well, it requires prior knowledge about the system and may not be very efficient in predicting the best structures since it does not search the entire space. As a result, it may fail to identify good structures that are vastly different from the starting structure.

On the other hand, the second approach involves the use of evolutionary algorithms that mimic Darwinian evolution to generate and select the best structures based on their given fitness while discarding the worst ones. In practical terms, this approach can be understood as a global search for minima in the multidimensional configuration space in which the algorithm zooms in on the most promising regions, eventually finding a list of local minima [50]. Since this study remains on fully theoretical grounds, not using any prior knowledge about possible structures, evolutionary algorithms presents itself as the best option for the task.

In the present work, the chosen implementation to perform the search was the USPEX code [51], which is an acronym for *Universal Structure Predictor: Evolutionary Xtallography*. As the name suggests, it is an evolutionary algorithm designed to predict the structure of the crystal based on its chemical composition. Like other evolutionary algorithms, USPEX mimics the process of biological evolution, treating crystal structures as individuals and applying the same dynamics used for biological individuals. The algorithm incorporates concepts such as generation and fitness and physical constraints are considered. In summary, the USPEX method can be broken down into three steps:

(1) The first generation is generated randomly. Each individual must follow hard constraints

related to the physics of the problem, such as minimal interatomic distance and minimum lattice vector length. If the individual does not follow the constraints, it is replaced with another that does. Each individual in the generation is then assigned a fitness, which represents the value that the algorithm seeks to minimize. In the present case, the fitness is the enthalpy per atom in the unit cell.

Enthalpy is a thermodynamic potential defined as the sum of the energy and PV, being P the pressure and V the volume of the system. In the performed USPEX calculations, the unit cell is allowed to relax without constraints, therefore achieving a value of null pressure. That is, energy and enthalpy are the same in the USPEX searches conducted in this work and will be treated as synonyms from now on.

(2) The individuals are relaxed using an external code. USPEX is interfaced with the main *ab initio* codes, such as VASP, SIESTA, Quantum ESPRESSO and others. This process consists in locally optimizing the structures according to their fitness values, effectively minimizing the energy to reach a local minima. The individuals with the worst fitness are discarded, while the remaining ones are used to produce the next generation of structures. The best individuals are replicated in the next generation, while variation operators are used to generate the rest of the structures.

The variation operators determine how the next generation of structures will be produced from the previous one. To mimic evolution, three biology-related concepts are chosen as operators: mutation, permutation and heredity. Mutation generates new structures by randomly changing the atomic coordinates and/or lattice vectors of the parent structure. Permutation involves swapping two or more atoms of the parent structure. Heredity, on the other hand, matches random slices from parent structures together to create a new structure. By using these operators, USPEX can preserve features from good structures while also exploring new and diverse structures. This approach helps to efficiently explore the large search space of crystal structures and identify promising candidates.

(3) The procedure of producing new generations is iteratively repeated until a convergence criterion is met. This criterion is related to the structure with the best fitness. Specifically, if the same structure is kept best for a user-defined number of generations, the simulation is terminated. The converged structure is then subjected to further relaxation using the same external code. This final structure can be considered as the predicted crystal structure of the given chemical composition, and its properties can be further explored.

After the USPEX search is completed, a variety of output files is generated. In addition to the best structure found, a list of other low-energy metastable structures discovered during the simulation is provided. These structures are also of great importance and need to be evaluated, since they correspond to other potential phases of the considered chemical composition. For example, Figure 2 shows the enthalpy of the best structure

for each generation until convergence for a MgSiO$_3$ chemical composition. The graph indicates that the perovskite and post-perovskite phases are found, which are both of significant importance.
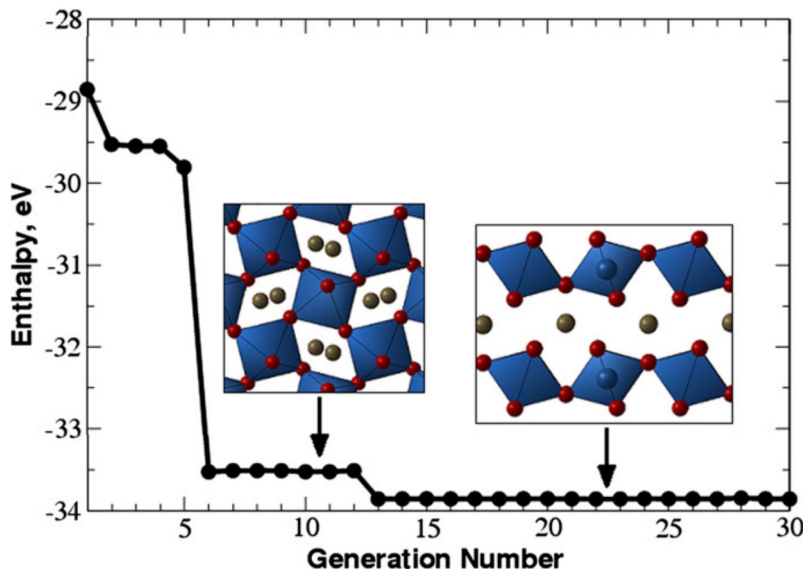
Figure 2 – Enthalpy of the best structure versus generation number for a population size of 30 individuals per generation. Calculation for a chemical composition of MgSiO$_3$ at 120GPa. Figure replicated from [50].

In summary, USPEX presents itself as an excellent method for conducting the search proposed in this study. It requires no prior knowledge of the structure, and its basic input includes only the chemical composition, the dimension of the crystal, and some parameters related to the structures, generations and variation operators. Once the convergence is reached, USPEX provides a list of low-energy phases for the given stoichiometry. With these promising crystal structures, stability and electronic properties can be calculated and other physical concepts can be evaluated. Therefore, the methodology chosen for this study begins using the USPEX code to search for structures with the lowest energies, followed by the assessment of a number of stability and electronic properties of the most promising candidates.

3.2   Arsenene allotropes: An example

To demonstrate the capabilities of USPEX as a crystal structure predictor, we present an example involving arsenene, the two-dimensional crystalline form of arsenic that has been extensively studied in its several phases [52, 53]. The objective is to investigate if USPEX can predict some of the known phases of arsenene.

To address this question, some parameters are set for USPEX to search for the desired structures. The primary consideration is the chemical composition. In the current case, we are searching for 2D structures composed solely of arsenic atoms. The search

range is set to include structures with a minimum of two and a maximum of sixteen arsenic atoms in the unit cell, ensuring a broad exploration of different geometries. Besides the chemical composition, it is essential to specify other parameters related to the way USPEX performs the search. These parameters describe not only the system that is being studied but also impact on the quality of the search and on the computational cost. Some of the most important parameters are considered below, while others are kept at their default settings:

```
Thickness = 5 Ang

Vacuum size = 15 Ang (distance between two adjacent slabs)

Population size = 30 individuals per generation

Initial population size = 30 individuals in the first generation

Best fraction = the 60% best structures of the current generation are used
to produce the next generation

Stop criterion = same structure kept best for 16 generations

The VASP package was employed to relax the structures over five steps, with
increasing precision of the parameters along the steps
```

In addition to those parameters, USPEX also allows the user to adjust the fraction of structures generated by each variation operator when constructing the next generation from the current one. As a reminder, the individuals in the first generation are created randomly and the following fractions were used to produce the subsequent generations:

```
50% of the structures were produced by heredity

30% of the structures were produced by random symmetric structure generator

10% of the structures were produced from lattice mutations

10% of the structures were produced from atomic coordinate mutations
```

For these specifications, a variety of structures were generated and their energies were evaluated. We selected the eight geometries with the lowest energies for further analysis, as depicted in Figure 3. Their energies in meV per atom can be found in Table 1.

Energy (meV/atom)							
(a)	(b)	(c)	(d)	(e)	(f)	(g)	(h)
0	18	48	72	87	114	131	147

Table 1 − Energy of structures (a)-(h), as indicated in Figure 3.

The results predicted by USPEX can be compared to the phases reported in the literature [52, 53]. Among the structures shown in Figure 3, the following geometries correspond to those mentioned in the referenced studies:
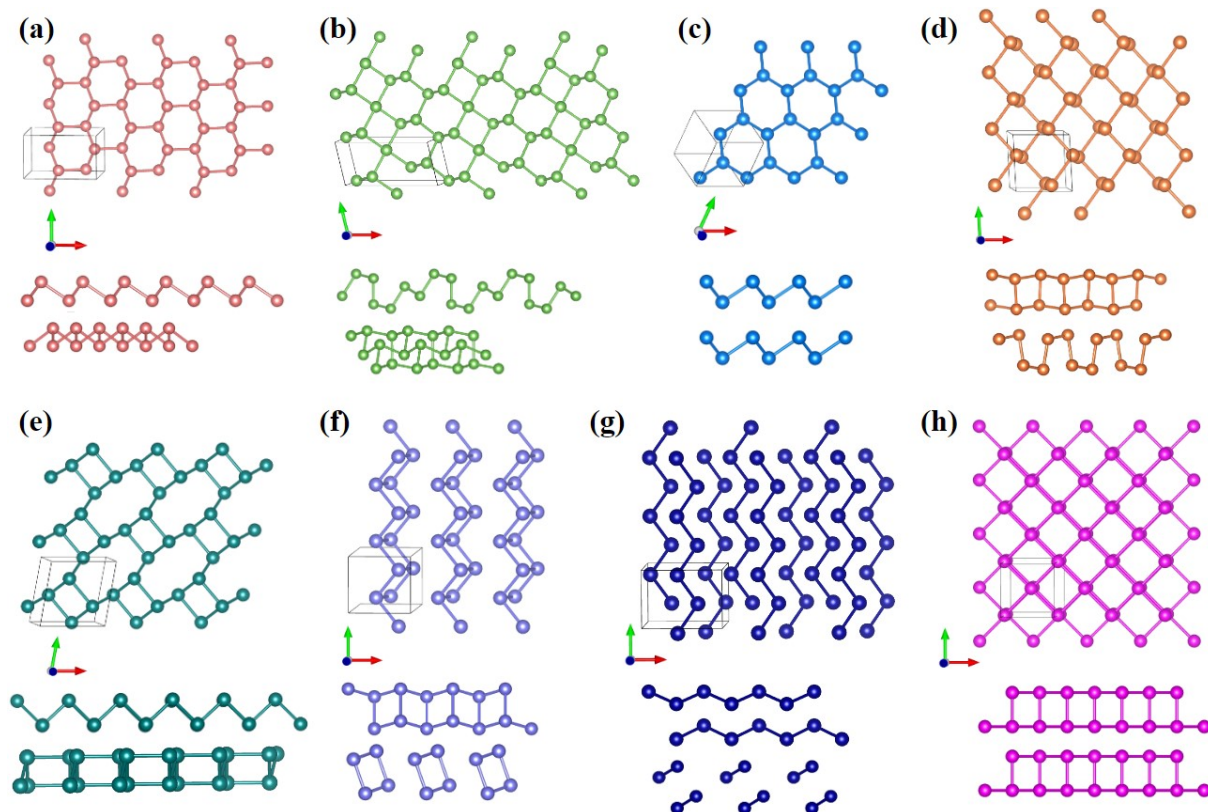
Figure 3 – Top and side views of the eight lowest-energy structures found by USPEX for the arsenene problem, in order of energy. The maximum length for As-As bonds is set to be 2.6 Å, a typical value for arsenic.

(a) matches ε from [53],

(c) matches β from [52],

(d) matches α from [52],

(e) matches ξ from [52],

(h) is similar to α from [52], but without vertical corrugation.

The results obtained from USPEX demonstrate good qualitative agreement with the expected geometries for arsenene allotropes. Although some structures predicted by USPEX were not identified in the considered references, it is important to note that the parameters were set to achieve a fast convergence, which may result in some loss of accuracy. These parameters can be refined for a more precise search if desired. However, the purpose of this example was to provide a qualitative understanding of the functionality of the tool, making the additional refinement unnecessary.

3.3 $B_2N_2O_2$: Structures found by USPEX

Returning to our main problem, in order to better understand the results obtained by USPEX, it is necessary to evaluate the parameters used in the search. The chemical

composition is $B_2N_2O_2$, meaning that the program will search for structures with two atoms of boron, two atoms of nitrogen and two atoms of oxygen in the unit cell. Similarly to the arsenene case, other parameters related to the way USPEX performs the search must be specified. The most relevant of them are provided below:

```
Dimension = 2D (slab)

Thickness = 10 Ang

Vacuum size = 22 Ang (distance between two adjacent slabs)

Population size = 20 individuals per generation

Initial population size = 20 individuals in the first generation

Best fraction = the 60% best structures of the current generation are used
to produce the next generation

Stop criterion = same structure kept best for 10 generations

The VASP package was employed to relax the structures over five steps, with
increasing precision of the parameters along the steps
```

The fraction of structures generated by each variation operator is set to be the same as in the arsenene case. For these parameters, the four lowest-energy structures found by USPEX are displayed in Figure 4. It is evident that the first two structures are similar, differing only in the way the nitrogen atoms are arranged between the top and bottom B-O networks. They both form a single connected 2D structure, few-angstroms thick, known as a slab, in contrast to the other two structures, in which N_2 molecules sublimated leaving parallel arrays of 1D boron oxide structures. Based on energetic aspects, only the first two structures were taken into consideration, disregarding the last two. Indeed, our criterion is to only keep structures whose total energies are within few tens of meV from the most stable. As presented in the insets of Figure 4, whereas the energy difference between structures 1 and 2 is smaller than that of kT at room temperature, this is not fulfilled by structures 3 and 4. We are using as reference for the energy the lowest value found, which will be described in the next subsection.

Structures 1 and 2, then, seem to be potential candidate to represent the outcome of the BN sheet oxidation, making it worthy to further investigate their properties. They are both slabs with rectangular symmetry, which means that the angle between their lattice vectors is approximately 90°. Whereas structure 1 displays a vertical-bond arrangement of nitrogen atoms, in structure 2 they form a linear zigzag pattern.

However, it remained uncertain if these were truly the best structures for the given chemical composition. To address this, another USPEX run was conducted, refining some parameters to obtain a more accurate search of the configuration space. This allowed for further comparison between the runs. Most of the parameters remained the same, with

1

ΔE = 4.1 meV/atom

2

ΔE = 19.1 meV/atom

3

ΔE = 43.2 meV/atom

4

ΔE = 71.2 meV/atom
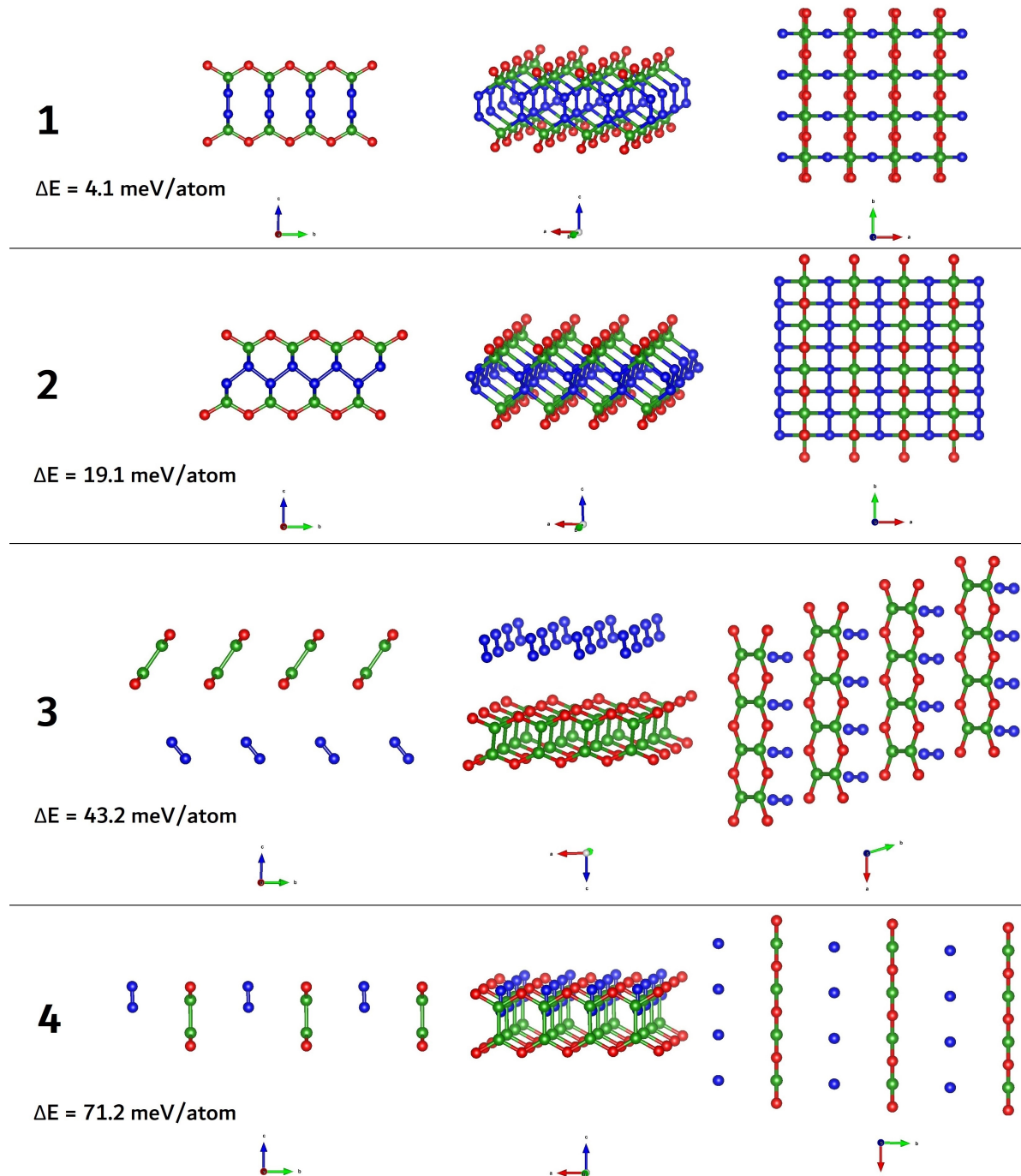
Figure 4 − The four lowest-energy structures found in the first USPEX run indicated from 1 to 4 in order of energy, where 1 is the lowest-energy structure. Green spheres depicts boron, blue depicts nitrogen and red depicts oxygen atoms. For visualization purposes, the unit cell is replicated in the x and y directions. Each structure is presented in three different perspectives.

only a few refined, which included:

```
Initial population size = 80 individuals in the first generation

Stop criterion = same structure kept best for 15 generations
```

This change of parameters prompt a change on the dynamics of the search. In the second

USPEX run, the initial population size was quadrupled compared to the first run. The motivation for that was to allow for a wider initial search of the configuration space, resulting in a more diverse first generation and the identification of a first best structure with a significantly lower energy. This, in turn, could lead to a faster convergence of the search. However, to ensure the reliability of the results, the stop criterion was updated to a higher value. Conducting this second run was crucial to compare the results and assess if the parameters used were adequate for delivering accurate results for the treated problem.

The four lowest-energy structures found in the second run are shown in Figure 5 along with the total energies found by USPEX integrated with VASP.

Structures 2 and 3 from the second run conspicuously also appeared as the second and third best structures in the first run. Similarly to the first run, structure 1 shows an analogous arrangement of boron and oxygen atoms as structure 2, differing only in the orientation of the nitrogen arrays. In this case, the lattice vectors are also different, as it can be seen in the third view of each structure in Figure 5. This new structure also possesses the same advantages as structures 1 and 2 from the first run, being a single connected 2D structure with an even smaller energy, making it ideal for this study. Structure number 4, as the fourth structure shown in Figure 4, represents an additional case in which the sublimation of N_2 molecules take place. As in the similar cases previously described, its total energy is relatively high and will not be further considered.

These results suggest that the refinement of the simulation parameters did not lead to a completely different family of structures. In fact, both runs produced the same second and third best structures, and the additional structure found was geometrically very similar to those observed in the first run. While it is possible to further refine the parameters, such refinements seem to not to lead to any significant improvement in the search for the best structure or other relevant metastable structures. Based on these findings, we selected three configurations to further investigate their properties, which are structures 1 and 2 of the first run, and structure 1 of the second run.

3.3.1   Selected structures for the study

After analyzing the results of the two USPEX runs, three structures were identified as suitable candidates for the present study. They are alike slabs, displaying a similar arrangement of boron and oxygen atoms but differing in the arrangement of nitrogen atoms. These three structures were selected for an in-depth investigation of their structural and electronic properties. The first step was to perform a second more careful relaxation making use of the SIESTA program [39].

SIESTA includes norm-conserving pseudopotentials [54, 55] and a numerical basis set composed of finite-range atomic orbitals. We chose the DZP basis set, which means 13
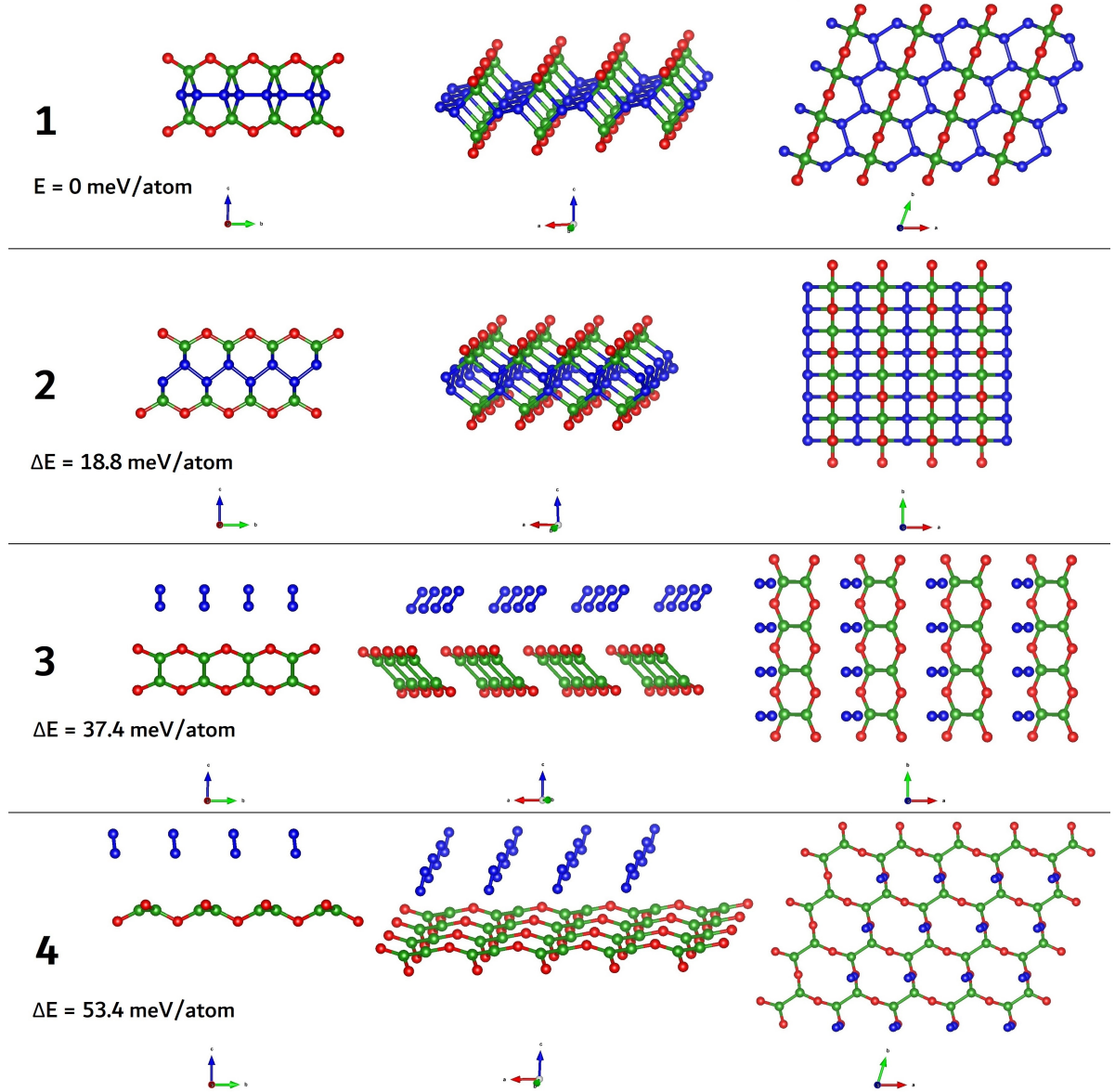
Figure 5 − The four lowest-energy structures found in the second USPEX run indicated from 1 to 4 in order of energy, where 1 is the lowest-energy structure. Green spheres depicts boron, blue depicts nitrogen and red depicts oxygen atoms. For visualization purposes, the unit cell is replicated in the x and y directions. Each structure is presented in three different perspectives.

functions for boron, oxygen and nitrogen atoms: two functions for each *s* and *p* orbitals in $n = 2$ level plus five *d-like* polarization orbitals. The exchange-correlation term in the Hamiltonian was treated within the Generalized Gradient Approximation (GGA) in the PBE parametrization [56]. The geometries were fully optimized with a convergence criterion of 0.005 eV/Å in the maximum force component of any atom. The grid was defined to sample the Brillouin zone by setting the parameter Kgridcutoff to 40 Å.

The structures are shown in Figure 6 along with their identification numbers. Values for the lattice parameters a and b and the angle γ between them can be found in
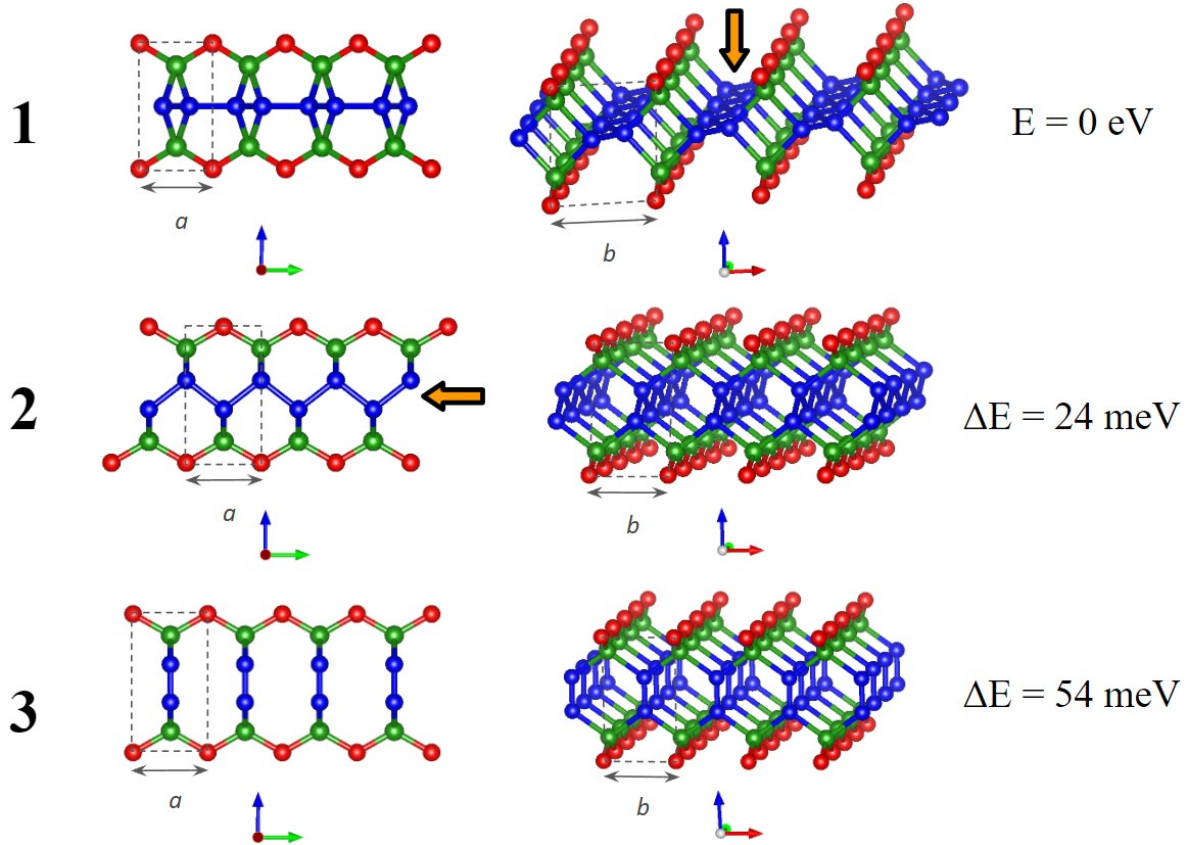
Figure 6 – The three structures selected for an in-depth study of its properties along with their energies per unit cell. Green spheres depicts boron, blue depicts nitrogen and red depicts oxygen atoms. For visualization purposes, the unit cell is replicated in the x and y directions. Each structure is presented in three different perspectives. Zigzag nitrogen arrays are indicated by orange arrows.

Table 2. Structure 1 had the lowest energy, followed by structures 2 and 3, respectively. Nitrogen zigzag arrays, present in the first two geometries, are indicated by orange arrows. This atomic configuration represents an intriguing aspect in the context of BN structures and, as we shall show, it will play an important role in defining the electronic properties of these structures. Their energy difference taking structure 1 as the reference can be found in the insets of Figure 6, which shows that the first two structures are degenerated within 4 meV/atom. Henceforth, the structures will be referred by their numbers as indicated in the figure.

Structure	a (Å)	b (Å)	γ
1	2.40	3.44	69.6°
2	2.41	2.74	90°
3	2.48	2.71	90°

Table 2 – Lattice parameters for structures 1, 2 and 3, as indicated in Figure 6.

<div align="right">

Chapter 4

</div>

Characterization of $B_2N_2O_2$

In this chapter, we aim to perform a theoretical characterization of the selected geometries obtained using USPEX, as described in the previous chapter. The structures are presented and labeled in Figure 6.

The characterization process is divided in two main parts. The first part concerns the structural properties of the geometries, while the second part explores their electronic properties. Subsequently, a simplified model using DFT is proposed to outline a potential path to the synthesis of these geometries using hexagonal boron nitride and oxygen as starting materials. At the end of the chapter, an extension of the results obtained with $B_2N_2O_2$ is discussed. The intention is to propose a family of structures exhibiting similar properties to those obtained with the original chemical composition. Some results are shown for a specific case, $Al_2As_2O_2$.

4.1   Structural properties

In order to evaluate the stability of the selected geometries, structural properties must be taken into account. Three calculations regarding stability features are performed: formation energy, phonon dispersion and molecular dynamics. They are discussed in more detail in the following subsections.

4.1.1   Formation energy

The formation energy is a crucial parameter that allows one to evaluate the likelihood of a structure to exist in nature. For systems in contact with pressure and temperature reservoirs, the equilibrium state is the one that minimizes the thermodynamic potential over the states consistent with the constraints. Since we are considering the particular case of fixed temperature and pressure, the ideal thermodynamic potential is given by the Gibbs free energy, which can be expressed as $G = \sum_i \mu_i N_i$.

In our case, we wish to compare two states, the proposed $B_2N_2O_2$ structure and the hexagonal boron nitride plus oxygen molecules, both in conditions of zero temperature and zero pressure, for which the Gibbs potential is equivalent to the total energy. The

formation energy can thus be defined as the energy difference between those two states:

$$E_{form} = E_{B_2N_2O_2}^{total} - \mu_{O_2} - 2 \cdot \mu_{BN},\qquad(4.1)$$

where N is the number of particles and the chemical potentials μ for O_2 and BN are simply the total energies of an O_2 molecule and the total energy per BN pair in hBN, respectively. The total energies are extracted from DFT calculations using the SIESTA package within the GGA-PBE approximation for the exchange-correlation potential, including the spin degrees of freedom. The total energy of $B_2N_2O_2$ was obtained using the same methodology. The resulting formation energies are as follows:

Structure	Formation Energy (E_{form})
1	-2.37 eV
2	-2.35 eV
3	-2.32 eV

A negative formation energy indicates that the energy of the structure at hand is lower than that of its constituents. In other words, energy would need to be supplied to break the structure into its components. Conversely, a positive formation energy implies that the energy of the structure broken into its constituents is lower than that of the structure itself. Since nature always searches for the minimum energy, a negative E_{form} is a desirable feature.

Fortunately, we found negative formation energies for all the considered structures, accounting for a value of approximately -0.40 eV/atom each, indicating a genuine stability. However, due to energetic considerations, from now on we focus solely on the characterization of structures 1 and 2, disregarding structure 3.

4.1.2 Phonon dispersion

We now shift our focus to the dynamic stability of the structures. We addressed this point by determining their phonon dispersion. The reasoning behind the fact that the phonon spectrum is a valuable tool for assessing the dynamic stability of a compound is discussed as follows.

Regarding the phonon modes as producing small displacements of the ions from their equilibrium positions, one possible outcome is the appearance of a restoring force. This is the case when the equilibrium starting point corresponds to a local minimum on the energy surface. Thus, the neighborhood of this point in the energy landscape has an upward concavity, which means that it will produce real frequencies in the spectrum. It is as if we were measuring the concavity by force constants k_{ij} and relating the frequencies to their square roots. On the other hand, if the outcome is a force pointing away from

the equilibrium starting point, by the same reasoning, it implies a maximum or saddle point in the energy landscape. This will tend to move the ions away from the equilibrium, indicating dynamic instability. Therefore, the signature of the instability will be imaginary frequencies, which will be represented in the spectrum as negative frequencies.

Having established the role of the phonon dispersion curves in our context, we now describe their determination within our first principles approach. The calculations were conducted using the SIESTA package within the GGA-PBE approximation. The mechanism for this calculation can be explained in two parts:

1. Supercell relaxation: A supercell consisting of 294 atoms was constructed for each structure. This involved replicating the optimized primitive cell of $B_2N_2O_2$ seven times along each lattice vector. The supercells were then relaxed using a convergence criterion of 0.02 eV/Å in the maximum force component of any atom. It is important to relax the structures using a tight maximum force criterion to ensure a precise calculation of the force constant matrix in the next step.

2. Phonon calculation: One primitive cell of $B_2N_2O_2$ within the supercell was selected and each of its six atoms was independently displaced along each of the x, y and z axes by 0.021 Å in both positive and negative directions. This procedure resulted in 36 distinct displacements as each of the six atoms was moved along $\pm x$, $\pm y$ and $\pm z$. The forces produced in each atom of the supercell by each displacement were calculated to generate the force constant matrix, which is finally diagonalized, resulting in the frequencies that are plotted in the phonon spectrum.

The frequencies are calculated along a specific path that connects the high symmetry points of the Brillouin zone for each structure. The paths can be seen in Figure 7. The phonon spectra for structures 1 and 2 are depicted in Figures 8 and 9, respectively. As previously discussed, imaginary frequencies in a spectrum, which are conventionally represented as negative frequencies in the phonon plot, are associated with instability points in the multidimensional energy surface, such as saddle points. Indeed, they are absent in Figure 9 and only small negative frequencies are observed in Figure 8, which can be ascribed to problems related to the lack of translational and rotational invariances caused by the supercell-size effects. These results indicate, therefore, dynamic stability of the structures.

4.1.3 Molecular dynamics

The next step in our stability tests consisted in performing molecular dynamics calculations at a fixed temperature. Thermal energy can be applied to drive the system out of a local minimum configuration, a phenomenon that may be captured by following the system at a constant temperature in its time evolution. To accomplish this, we carried out molecular
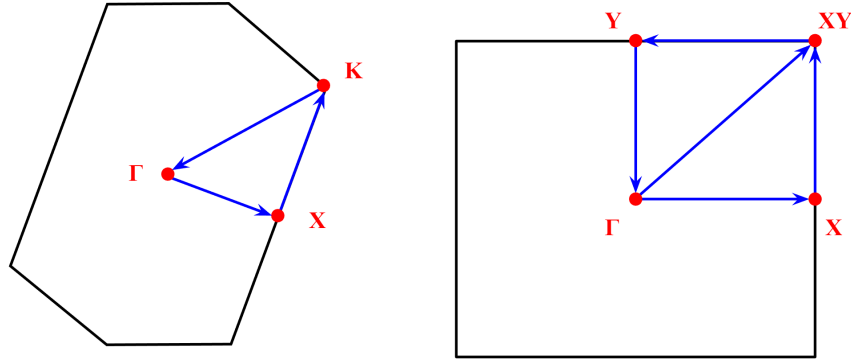
Figure 7 – Brillouin zone of structures 1 (left) and 2 (right), indicating the high symmetry points and the k-path used for calculation of the phonon spectra.
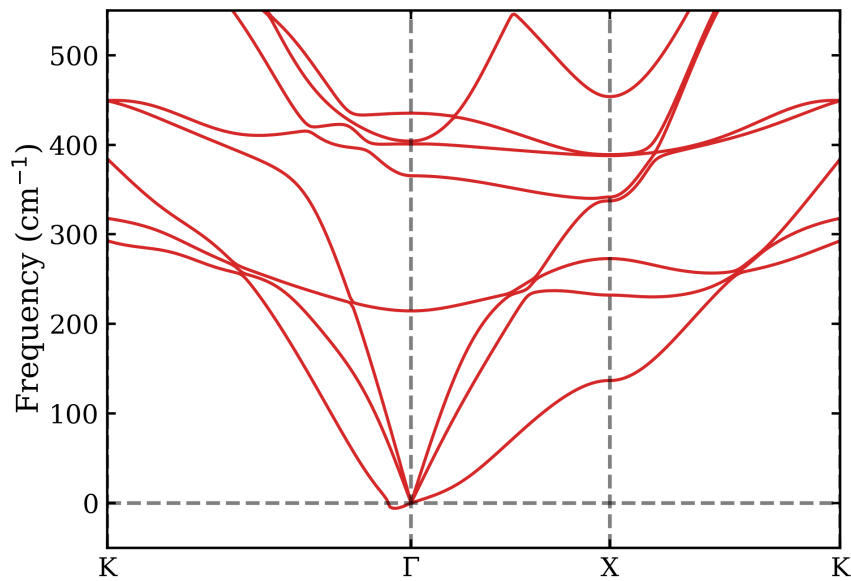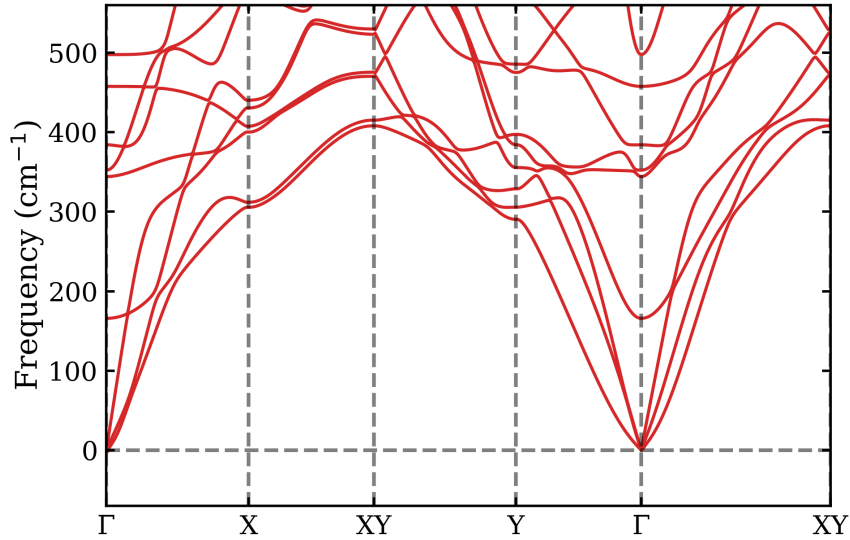

Figure 8 – Phonon dispersion plot for structure 1. The k-path used for the calculation is indicated in Figure 7.

dynamics simulations within the DFT-GGA formalism using the SIESTA implementation.

The employed system consisted of a 216 atoms supercell built from the replication of the primitive cell six times along each lattice vector on the plane. The calculations were performed making use of the Nosé scheme to generate trajectories in the canonical ensemble. For that, we set up a Nosé mass of 150 Ry fs^2 and a high average temperature of 600 K.

The molecular dynamics calculations for structures 1 and 2 were conducted for approximately 5 ps, using 1 fs as the time step, and we did not observe any significant structural change during the total time of the simulations. These results characterize the structures as thermally stable.

Figure 9 – Phonon dispersion plot for structure 2. The *k*-path used for the calculation is indicated in Figure 7.

4.2 Electronic and transport properties

In this section, we perform an electronic characterization of the selected geometries to gain insights into their electronic structure and transport properties. By examining the electronic states and estimating the electron and hole mobilities, we can obtain valuable information about the behavior of carriers under an applied electric field and identify potential applications. The following subsections provide a detailed analysis of these aspects.

4.2.1 Electronic states

To characterize the electronic states of the structures at hand, we performed three calculations: band structure, projected density of states (PDOS) and localized density of states (LDOS).

The band structure and projected density of states onto each element were obtained using DFT calculations conducted with the VASP program. We used a plane-wave cutoff of 450 eV. Initially, both calculations were performed within GGA in the PBE parametrization. However, given the well-known tendency of the GGA functional to underestimate the band gap, we also employed HSE06 hybrid functional [57, 58] in band structure calculations to achieve a more accurate characterization of the electronic states. Figures 10 and 11 show the band structure (PBE and HSE) and PDOS (PBE) for structures 2 and 1, respectively.

Both calculations yield approximately the same qualitative features for the bands. In Figure 10, a direct band gap at the Γ point is predicted, but the HSE06 correction significantly enhances the band gap from 1.66 to 3.41 eV. The results observed in Figure

11 follow a similar pattern: the band gap increases from 2.11 to 3.81 eV in the HSE06 result. The main difference is that the band gap of structure 1 becomes indirect, with the top of the valence band at the Γ point and the bottom of the conduction band at the X point.
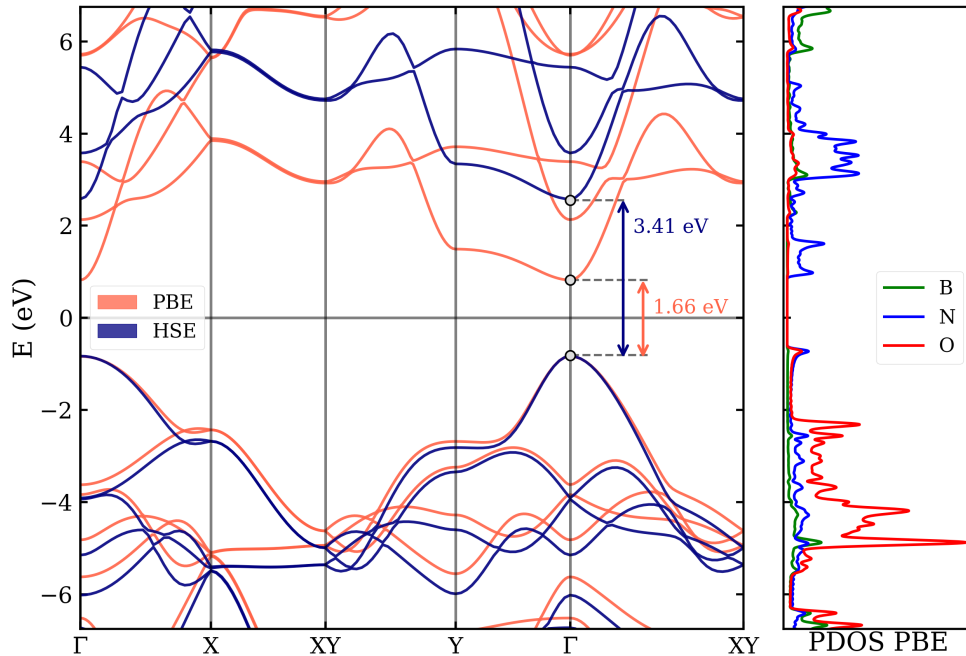
Figure 10 − Band structure for structure 2. The Fermi level is set to zero. The k-path used for the calculation is indicated in Figure 7.
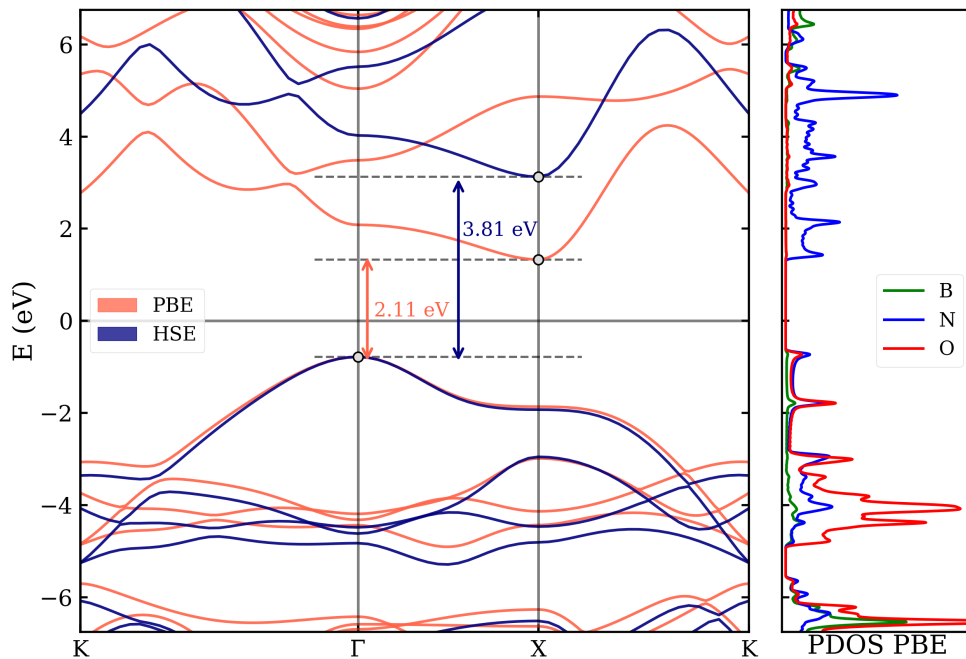

Figure 11 − Band structure for structure 1. The Fermi level is set to zero. The k-path used for the calculation is indicated in Figure 7.

These results classify structures 1 and 2 as wide-bandgap (WBG) semiconductors. In both cases, the top of the valence band and bottom of the conduction band are nearly

parabolic. The bottom of the conduction band is predominantly localized in the nitrogen zigzag array, while the top of the valence band is split between oxygen and nitrogen atoms, as shown in the projected density of states. The LDOS isosurface plots in Figures 12 and 13 provide a visual representation of the electronic density at the top of the valence band and the bottom of the conduction band for structures 2 and 1, respectively. These calculations were conducted using the SIESTA package with an energy range of 0.3 eV and 0.1 eV for the valence and conduction band edges, respectively.

The hybridization of valence states between oxygen and nitrogen orbitals promoted by the nitrogen channels is an important result in the present case. These arrays are completely responsible for the low-energy conduction states and, as we shall show, have a profound effect on the electron and hole mobilities. This set the considered structures apart from many oxide WBG materials, which often suffer from low mobilities, specially for hole carriers, due to the localized character of oxygen $2p$ orbitals [59].
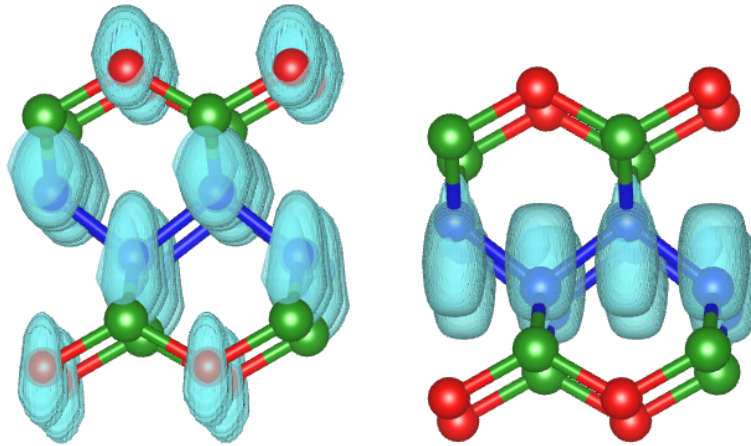
Figure 12 – Isosurface plots of the electronic density of structure 2 for the valence band edge (energy range of 0.3 eV) and for the conduction band edge (energy range of 0.1 eV).
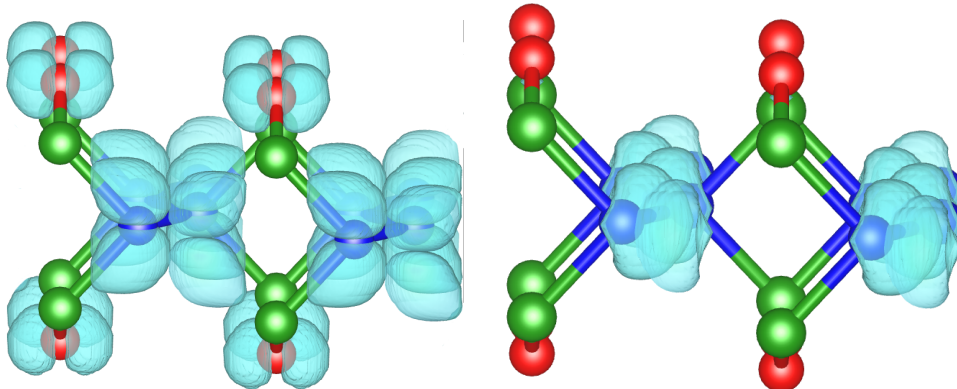
Figure 13 – Isosurface plots of the electronic density of structure 1 for the valence band edge (energy range of 0.3 eV) and for the conduction band edge (energy range of 0.1 eV).

4.2.2 Carrier mobility

The carrier mobility is a property that measures how quickly carriers move in the material when an external electric field is applied. The higher the mobility, the faster the carriers move. In this study, carrier mobilities were calculated in the framework of the deformation potential [60, 61], which is formulated within the method of the effective mass.

This method first took place in the context of Wannier functions, which, in turn, were introduced to simplify the problem of perturbed systems, such as semiconductors with defects. When applied to the Schrödinger equation, these functions generate a simplification on the description of the problem, since all information about the band structure appear in one single term. The effective mass emerges as a local approximation to the band structure, which takes a parabolic shape near the edges. The idea is to locally treat the bands as those of a free electron with an effective mass m^*. This concept is widely applied in condensed matter problems, including mobility calculations within the deformation potential framework. This approach is based on applying deformations on the lattice, which generate potentials (the deformation potentials). These terms are then added to a Schrödinger-like equation written within the framework of the effective mass.
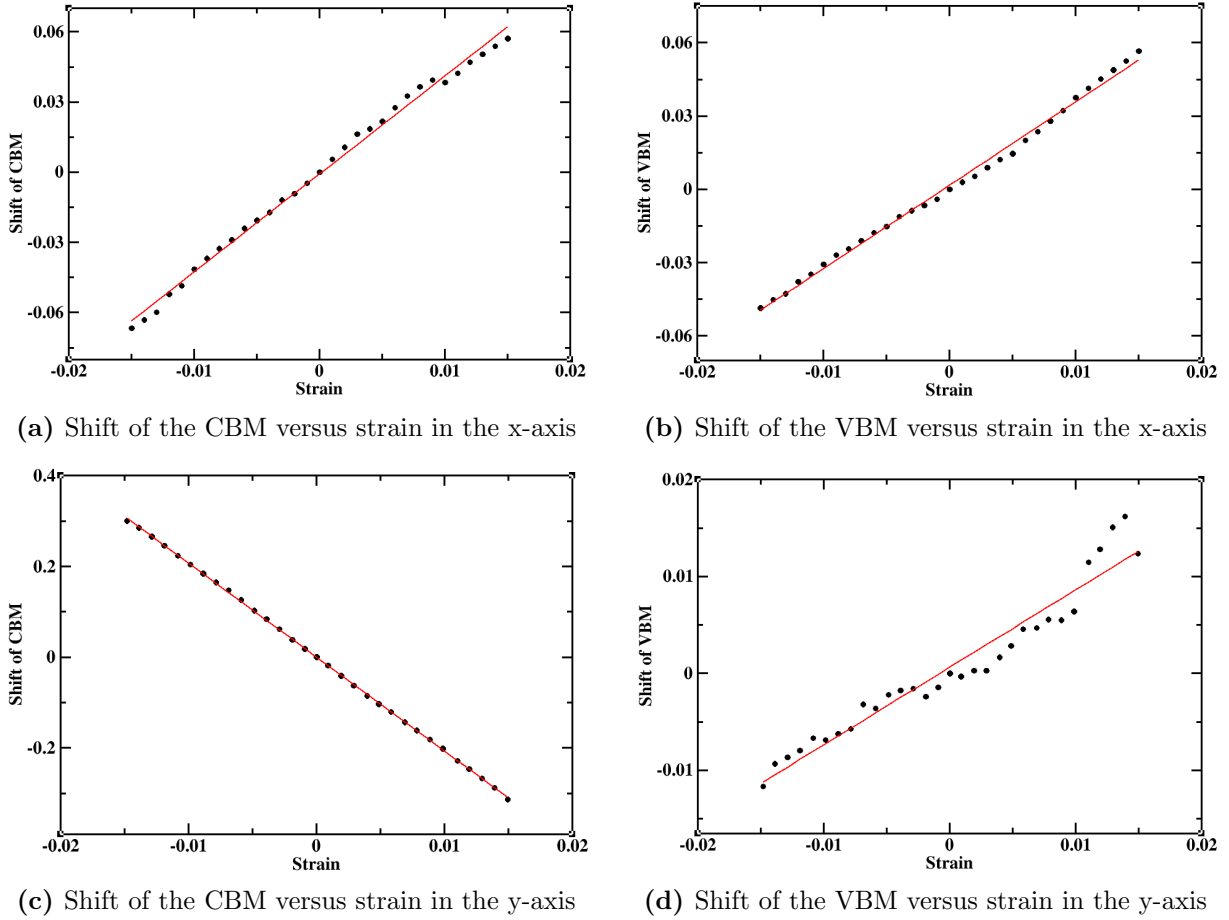
The deformation potential approach considers the scattering of carriers due to phonons as the mechanism limiting the conduction. Long-wavelength phonons are simulated by application of strain in two orthogonal directions, and the deformation potential, related to the electron-phonon coupling, is determined based on the calculated shifts in the valence and conduction band edges.

The determination of the actual mobilities, taking into account all possible sources of scattering, is beyond the scope of the present work. Here, we focus only on the phonon-limited scattering model to show that this mechanism yields relatively high contributions for the mobilities, largely due to the existence of the nitrogen electronic channels.

In our calculations, carried out with the SIESTA code, we applied strain in the x and y directions in steps of 0.1%, ranging from -1.5% to 1.5%, relaxing the coordinates in each step. The deformation potential E_d^i was estimated as $E_d^i = \Delta V_i / \varepsilon$, in which i stands for conduction or valence band edge, ΔV_i is the energy shift of the ith band under cell deformation and ε is the strain ($\varepsilon = \Delta l / l_0$). In terms of E_d^i, and assuming $T = 300$ K, the 2D mobility is given by [52, 62, 63]:

$$\mu_{2D} = \frac{e\hbar^3 C_{2D}}{k_B T m_j^* m_a (E_d^i)^2}.$$

(4.2)

The effective masses m_j^* along the directions specified by j (either x or y) were calculated with the second derivatives of the band energy evaluated in the band edges, and m_a is an average effective mass, given by $\sqrt{m_x^* m_y^*}$. This calculation is justified by the nearly parabolic nature of the bands in the proximity of the conduction and valence band edges,

(a) Shift of the CBM versus strain in the x-axis

(b) Shift of the VBM versus strain in the x-axis

(c) Shift of the CBM versus strain in the y-axis

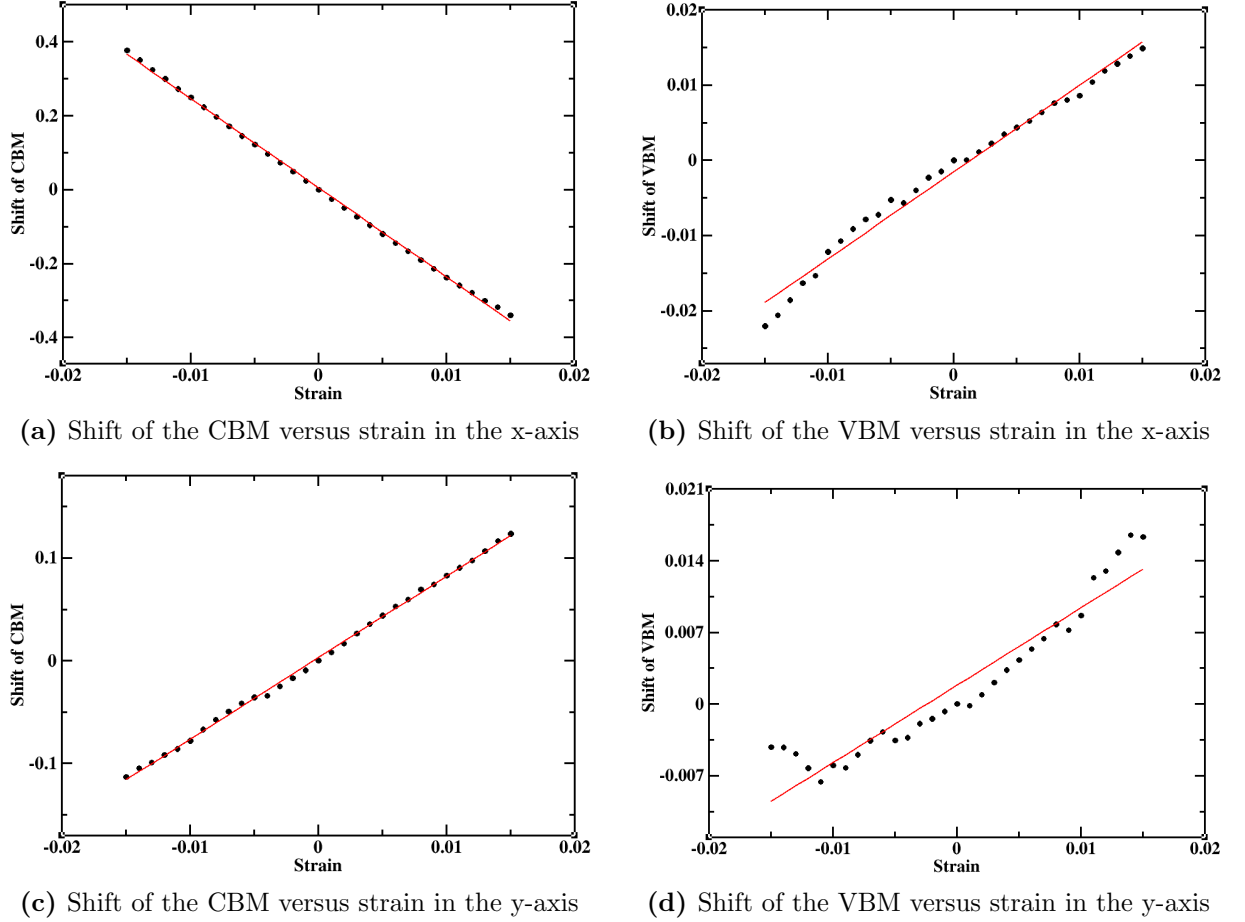(d) Shift of the VBM versus strain in the y-axis

Figure 14 – Shift of the valence band minimum (VBM) and conduction band maximum (CBM) of structure 1 under strain in the x and y directions. The slope of the graphs are used to calculate the deformation potentials E_d^i. The red line is the linear fitting of the results.

which allows us to write:

$$E(k) = \frac{\hbar^2 k^2}{2m_j^*},$$

in these regions. Finally, C_{2D} represents the elastic modulus along the transport direction. When small deformations are applied on a lattice, it is expected its total energy to increase with the square of the deformation - it is the phenomenon we see, for instance, in the most classical physics problem: the harmonic oscillator. In the present case, C_{2D} was calculated assuming the parabolic fitting $(E - E_0)/S_0 = \varepsilon^2\, C_{2D}/2$ of the energy difference $E - E_0$ as a function of the strain ε, and defining S_0 as the area of the unit cell in equilibrium.

We applied 30 different deformation percentages in each direction independently, keeping the deformed lattice coordinate fixed and allowing the remaining ones to relax along with the atomic coordinates with a criterion of 0.003 eV/Å in the maximum force component. This caused linear shifts in the conduction band maximum (CBM) and valence band minimum (VBM), from which we extracted the deformation potentials E_d^i ($i = x, y$) as the slope of the plots. The shifts of the band edges under deformation versus applied

(a) Shift of the CBM versus strain in the x-axis

(b) Shift of the VBM versus strain in the x-axis

(c) Shift of the CBM versus strain in the y-axis

(d) Shift of the VBM versus strain in the y-axis

Figure 15 − Shift of the valence band minimum (VBM) and conduction band maximum (CBM) of structure 2 under strain in the x and y directions. The slope of the graphs are used to calculate the deformation potentials E_d^i. The red line is the linear fitting of the results.

strain are depicted in Figures 14 and 15 for structures 1 and 2. The total energy vs. strain plot, on the other hand, show the described parabolic tendency and are presented in Figure 16 for both structures as well. The described parameters along with the calculated mobilities are displayed in Table 3.

Table 3 − Calculated electron and hole mobilities, C_{2D}, deformation potential and effective masses relative to the electron mass m_0 for structures 1 and 2 with applied strain over directions x and y.

St.	Dir.	C_{2D} (J/m²)	Electron			Hole		
			E_d^i (eV)	m_α^*/m_0	μ_α (cm²/V·s)	E_d^i (eV)	m_α^*/m_0	μ_α (cm²/V·s)
1	x	242	4.19	0.352	4.97·10³	3.41	0.295	4.59·10³
	y	458	20.71	0.081	1.67·10³	0.80	0.364	1.28·10⁵
2	x	581	24.07	0.078	1.49·10³	1.15	0.567	5.33·10⁴
	y	242	7.93	0.440	5.70·10³	0.76	0.166	5.18·10⁴

The contributions to the electron mobilities for both geometries and deformation directions were found to be in the range of 10^3 cm²/V·s and are higher than that of widely used semiconductors such as silicon and MoS$_2$, with a mobility of 1400 and 200 cm²/V·s,

respectively [64]. Furthermore, hole mobilities were found to be even higher, ranging from 10^3 to 10^5 cm^2/V·s, which is comparable to the mobility of graphene, a material known for its exceptionally high carrier mobilities.

These values should be viewed only as an upper bound for the actual mobilities, since we have neglected other sources of scattering. However, it is an important result in the context of WBG oxides, showing that the proposed $B_2N_2O_2$ geometries may overcome limitations imposed by the localization of oxygen $2p$ orbitals in conduction mechanisms. We attribute these results to their main structural feature, which is the existence of the zigzag arrays of nitrogen atoms, as it was discussed and observed in the results shown in the previous section.
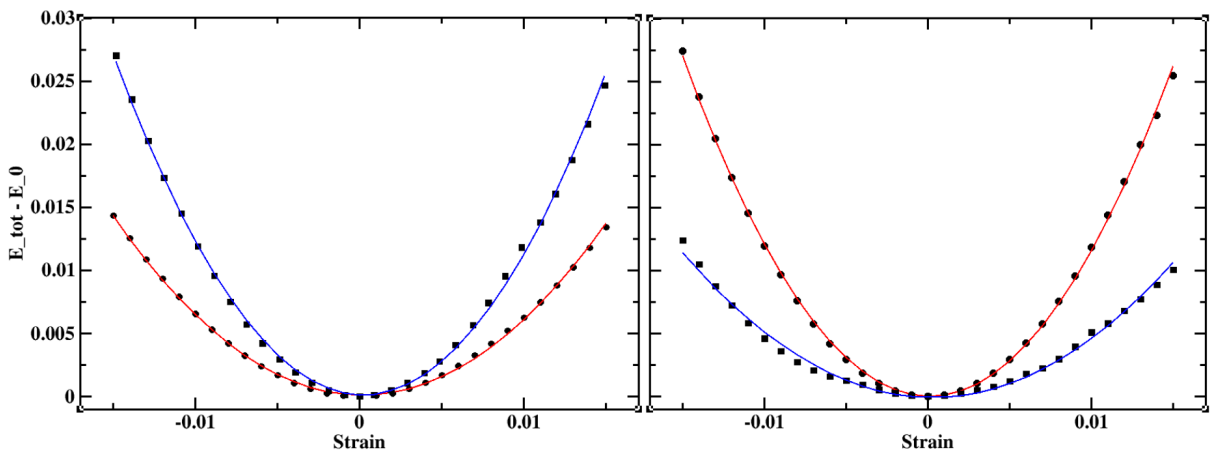
Figure 16 – Shift of the total energy versus strain for structures 1 (left) and 2 (right). Circles represent the measured shifts for strain in the x direction (red fitting) and squares for strain in the y direction (blue fitting). The quadratic coefficient is used to calculate the elastic modulus C_{2D}.

4.3 A possible route to $B_2N_2O_2$

Having established several properties of the proposed compounds, we now address a fundamental point: How could the structures be synthesized? Details of chemical reactions which could show how specific molecules would interact with hBN layers to generate $B_2N_2O_2$ compounds are beyond the scope of the present work and would doubtfully be accessible in a DFT calculation. However, it is possible to identify general trends leading to the formation of these final structures. The aim of this section is to outline these trends.

To investigate the synthesis process, we carried out a two-step calculation. In the first part, we assumed that an oxygen-rich environment interacting with a BN layer may produce a complete functionalization of the boron atoms. Hence, we set up a relaxation calculation for an initial structure defined by a hBN layer, represented by a rectangular unit cell with two B and two N atoms, in which one O atom was placed atop one B atom,

and another O atom below the other B atom. The distance between oxygen and both boron and nitrogen was set to be consistent with a covalent bond of approximately 1.5 Å.

The relaxation led to a metastable structure, shown in Figure 17 (a), with a total energy of 3.10 eV per primitive cell taking structure 1 as reference. In the relaxed geometry, the O atoms made bonds with B and N atoms above and below the plane, adopting a bridged configuration while preserving the B-N bonds. The rectangular primitive cell have lattice vectors $(a, 0, 0)$ and $(0, b, 0)$ with $a = 4.55$ Å and $b = 2.64$ Å.

In the second step, we performed a series of calculations in which the lattice parameter a was decreased by 0.2 Å in each run, while allowing the atomic positions to relax in a fixed cell. These calculations mimic the application of a uniaxial pressure in the structure. For each configuration, we carried out an additional calculation with a full optimization, including the lattice vectors. After going through the intermediate geometry illustrated in Figure 17 (b), the metastable oxidized BN sheet evolved firstly into structure 3, as shown in Figure 17 (c). The shrinkage process continued until the constrained lattice length a reached 2.9 Å, at which point the geometry transitioned into structure 2, as depicted in Figure 17 (d).
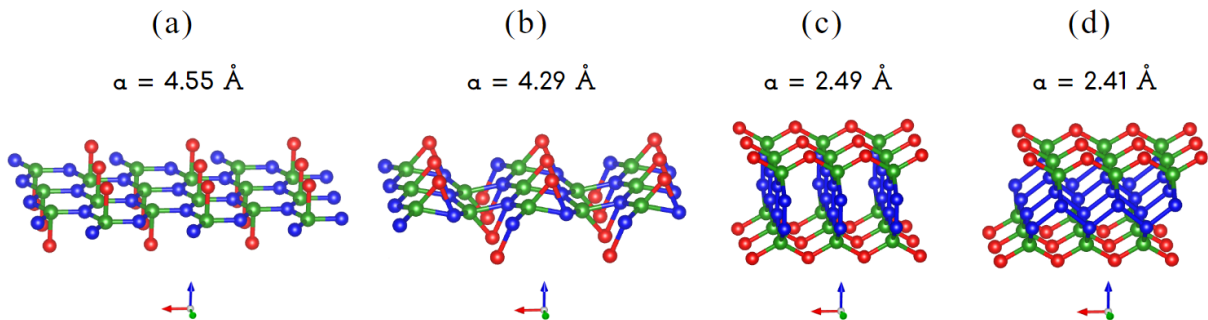
Figure 17 – The four steps of the proposed scheme for the synthesis of $B_2N_2O_2$ from the oxidation of hBN. Increasing pressure is applied from (a) to (d), with (d) being structure 2. The relaxed parameter a is indicated for each step.

These results suggest a plausible scheme in which structure 2 is obtained through the oxidative process of hBN combined with application of pressure. Based on these findings, our subsequent focus will be directed towards this particular geometry, which will serve as a basis for proposing an extension of the discussed results to a family of structures.

4.4 A family of structures

In the preceding sections, we thoroughly explored various aspects of the most promising geometries for the oxidation of a BN sheet. From investigating their structural and electronic properties to proposing a synthesis scheme that yields one of the structures, we have gathered convincing evidence of the interesting properties exhibited by $B_2N_2O_2$

compounds. These properties characterize them as desirable for numerous applications, making it worth further investigation.

In this context, we propose the exploration of new structures that possess the same geometry and a similar chemical composition to $B_2N_2O_2$. The idea is to substitute boron and nitrogen with other elements found in the same columns of the periodic table, as these elements exhibit similar chemical behaviors to their original counterparts.
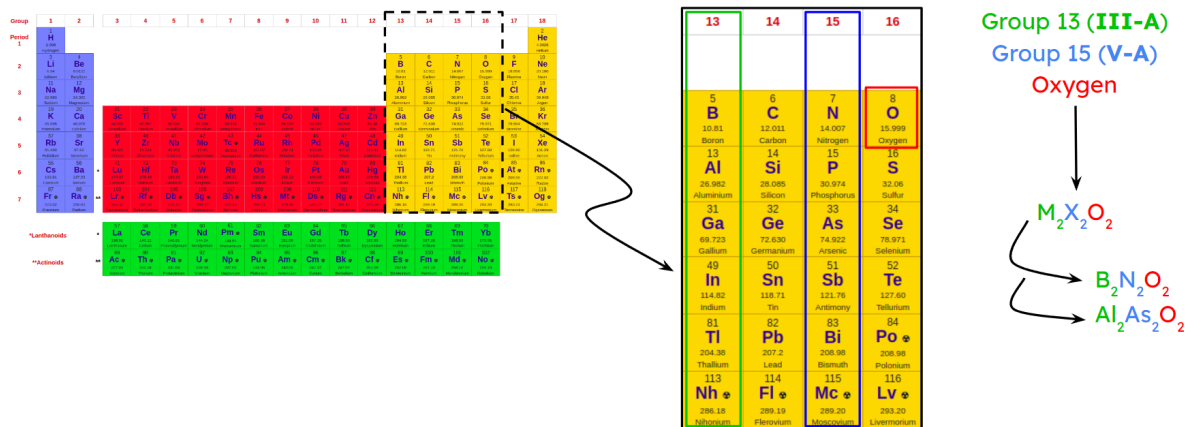

Figure 18 – Schematic representation of the arrangement proposed for the family of structures based on $B_2N_2O_2$. The periodic table of elements is shown with a highlight of columns 13-16, and some examples are given.

A convenient way to describe members of this family is by setting the general chemical composition $M_2X_2O_2$, where M represents an element from group 13 and X an element from group 15. Figure 18 provides an illustrative representation of this scheme. $Al_2As_2O_2$, $Ga_2Sb_2O_2$ and $In_2As_2O_2$ can be cited as members of the family, for instance.

Among the mentioned structures, we opted to conduct an in-depth investigation of one specific member of this proposed family: $Al_2As_2O_2$. This composition results from the substitution of boron with aluminium and nitrogen with arsenic. Following a similar methodology to that employed for $B_2N_2O_2$, a simplified characterization was performed to provide insights into the properties of this new material.

4.4.1   Geometry

Before delving into the properties of $Al_2As_2O_2$, the atomic and lattice parameters of this compound must be specified. The first step is to substitute boron with aluminium atoms and nitrogen with arsenic atoms in the geometry of structure 2, which can be found in Figure 6. A relaxation calculation is then conducted using the SIESTA package with a Kgridcutoff of 40 Å and a maximum force component of 0.005 eV/Å. It is crucial to perform this calculation, since interatomic distances and lattice vectors change with the elemental substitutions. The relaxed lattice vectors were found to be $(a, 0, 0)$ and $(0, b, 0)$ with $a = 3.327$ Å and $b = 4.473$ Å. The optimized structure is illustrated in Figure 19.
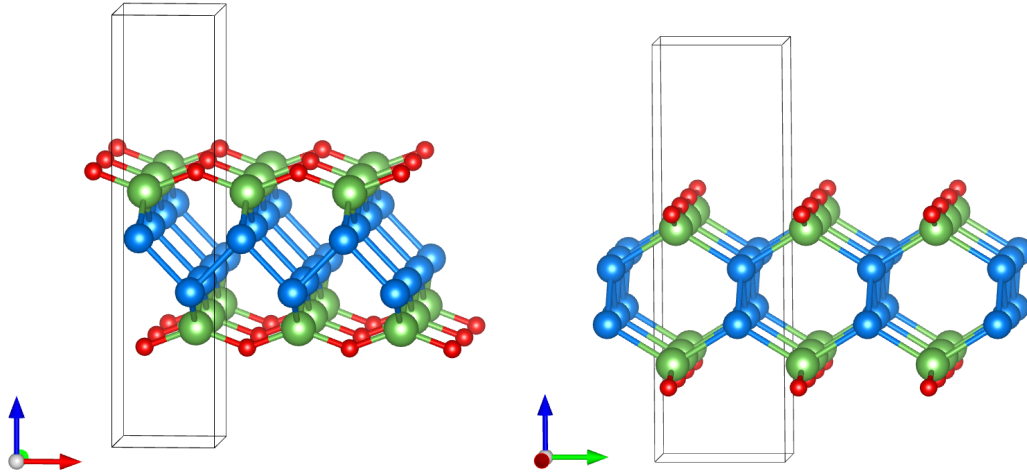
Figure 19 – Relaxed geometry of $Al_2As_2O_2$, an analogous of structure 2 from Figure 6.

4.4.2 Structural properties

Having defined optimized atomic coordinates and lattice vectors for $Al_2As_2O_2$, we can evaluate structural properties. Our focus is to outline two stability properties in this subsection: formation energy and phonon spectrum.

In contrast with the BN counterpart, an hexagonal AlAs sheet does not exist in nature. Therefore, the formation energy of $Al_2As_2O_2$ is calculated taking bulk zincblende AlAs and molecular O_2 as reservoirs of Al, As and O atoms. Considering the chemical potentials μ_{AlAs} and μ_{O_2}, the formation energy is calculated as:

$$E_{form} = E_{Al_2As_2O_2}^{total} - \mu_{O_2} - 2 \cdot \mu_{AlAs} \tag{4.3}$$

Both the chemical potentials and the total energy were extracted from DFT calculations conducted using the SIESTA package within the GGA-PBE approximation. The resulting formation energy of $Al_2As_2O_2$ was calculated to be -6.08 eV, accounting for -1.01 eV/atom, a negative value that, as previously discussed, is a desired feature that indicates stability.

The phonon dispersion is calculated following the methodology and the same parameters as described in Subsection 4.1.2. The resulting phonon spectra is illustrated in Figure 20, showing no negative frequencies and therefore indicating dynamic stability of the compound.

4.4.3 Electronic properties

In this subsection, we explore the electronic properties of $Al_2As_2O_2$, including the calculation of the band structure, projected density of states (PDOS) and carrier mobility.

The band structure and PDOS calculations were conducted with the VASP program using a plane-wave cutoff of 400 eV. We employed two approximations for the
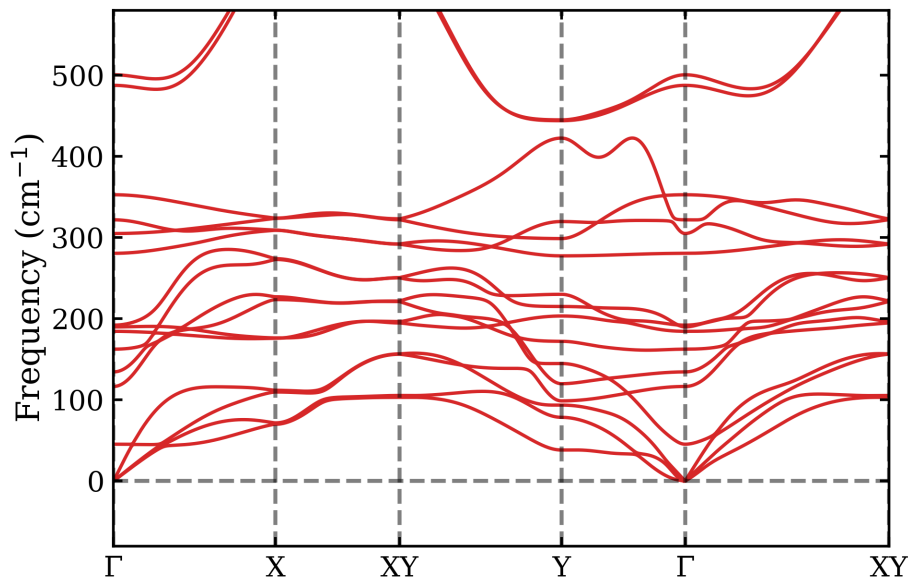
Figure 20 − Phonon dispersion plot for $Al_2As_2O_2$ in the geometry depicted in Figure 19. The k-path used for the calculation is indicated in the right-hand side of Figure 7.

exchange-correlation functional: GGA-PBE and HSE06. The resulting band structure is shown in Figure 21.
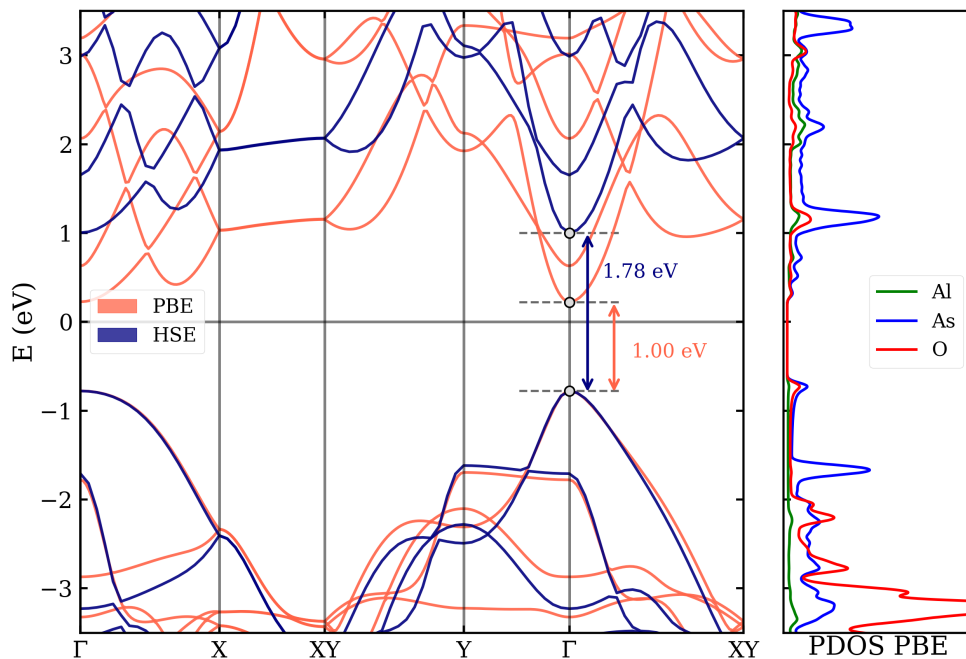
Figure 21 − Band structure for $Al_2As_2O_2$ in the geometry depicted in Figure 19. The k-path used for the calculation is indicated in the right-hand side of Figure 7.

Both approximations exhibit qualitatively similar band features, indicating a direct band gap at the Γ point. However, the HSE conduction bands are shifted upwards relative to the PBE bands, generating a correction of the gap: it enhances from 1.00 eV to 1.78 eV.

The projected density of states of the highest-energy valence band demonstrates

(a) Shift of the CBM versus strain in the x-axis

(b) Shift of the VBM versus strain in the x-axis

(c) Shift of the CBM versus strain in the y-axis
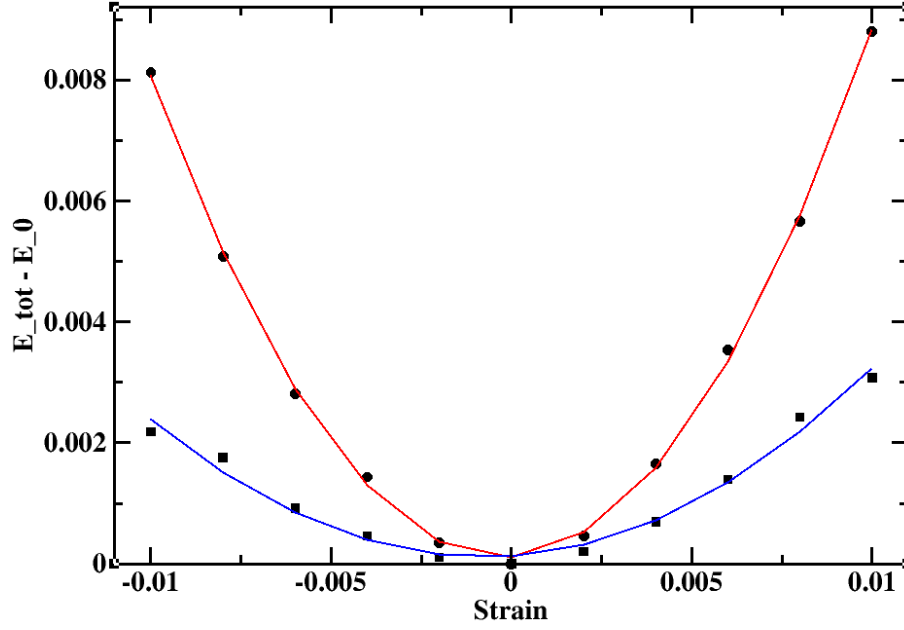

(d) Shift of the VBM versus strain in the y-axis
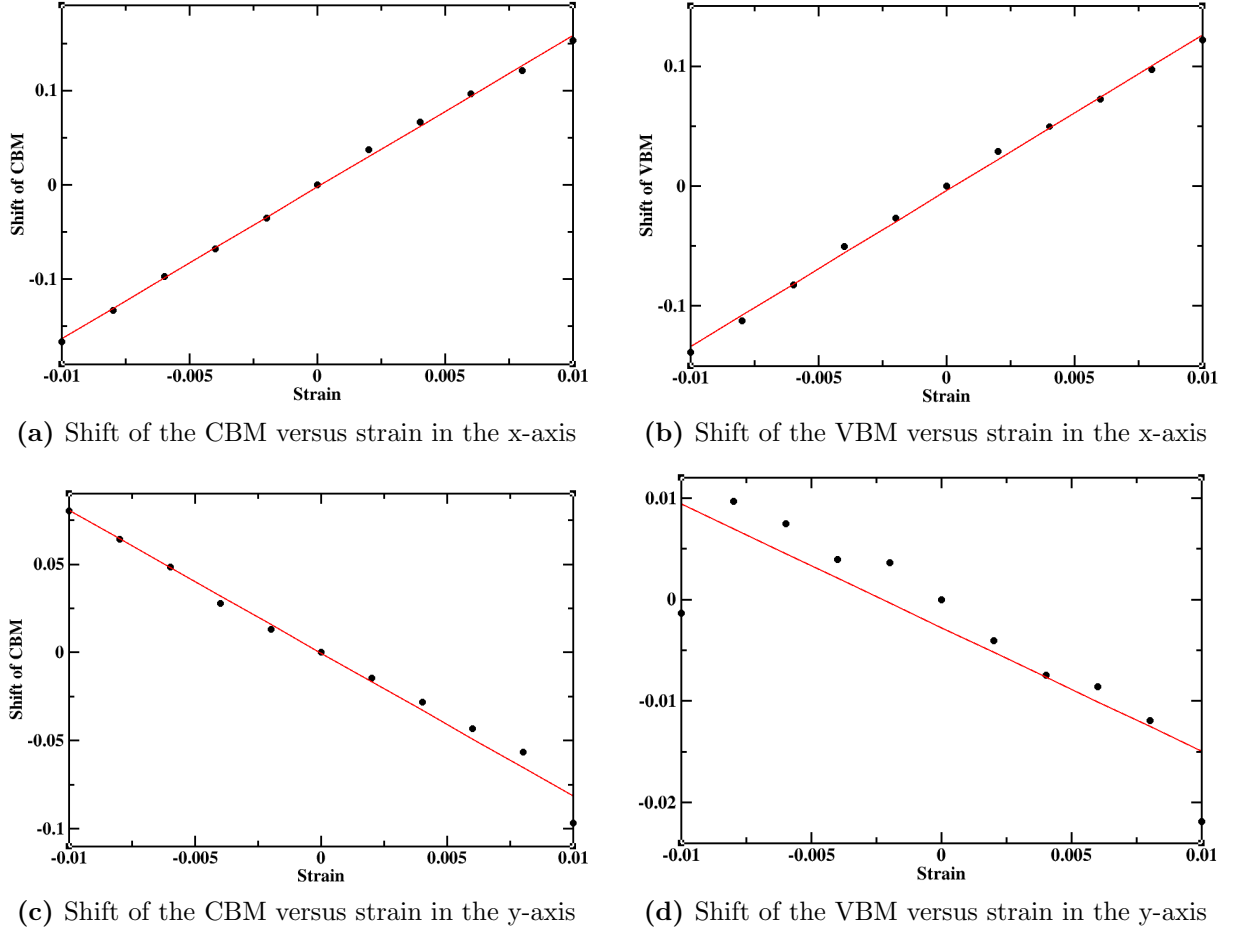
Figure 22 – Shift of the valence band minimum (VBM) and conduction band maximum (CBM) of $Al_2As_2O_2$ under strain in the x and y directions. The slope of the graphs are used to calculate the deformation potentials E_d^i. The red line is the linear fitting of the results.

similarities to the $B_2N_2O_2$ cases, with contributions from both arsenic and oxygen orbitals. In contrast, the lowest-energy conduction band, although showing a main contribution from the arsenic orbitals, also exhibits smaller contributions from aluminium and oxygen.

Carrier mobilities were calculated in a similar manner to $B_2N_2O_2$, with strain along the x and y directions. However, deformations were applied in steps of 0.2%, ranging from -1.0% to 1.0%, resulting in ten different deformation percentages. All calculations were carried out with SIESTA within the GGA framework. The data obtained for the calculation of deformation potentials and elastic moduli are presented in Figures 22 and 23. Table 4 summarizes the parameters and the resulting electron and hole mobilities for $Al_2As_2O_2$.

The calculated electron and hole mobilities were found to be in the range of 10^2 cm²/V·s, except for the hole mobility with strain applied over the y axis, that was found to be one order of magnitude higher. Even though the carrier mobility of $Al_2As_2O_2$ is lower than that of the BN counterpart, it is still comparable to the mobility of the widely used

Figure 23 – Shift of the total energy versus strain for $Al_2As_2O_2$. Circles represent the measured shifts for strain in the x direction (red fitting) and squares for strain in the y direction (blue fitting). The quadratic coefficient is used to calculate the elastic modulus C_{2D}.

Table 4 – Calculated electron and hole mobilities, C_{2D}, deformation potential and effective masses relative to the electron mass m_0 for $Al_2As_2O_2$ with applied strain over directions x and y.

Dir.	C_{2D} (J/m²)	Electron			Hole		
		E_d^i (eV)	m_α^*/m_0	μ_α (cm²/V·s)	E_d^i (eV)	m_α^*/m_0	μ_α (cm²/V·s)
x	184	16.06	0.405	$2.40 \cdot 10^2$	13.00	0.659	$1.34 \cdot 10^2$
y	59	8.11	0.060	$3.02 \cdot 10^2$	1.22	0.104	$4.90 \cdot 10^3$

semiconductors silicon and MoS_2. Indeed, the decrease on the electron mobilities can be a consequence of the higher contribution of other elements in the valence band, as observed in the PDOS. However, as described in Subsection 4.2.2, this approximation considers only the scattering of carriers due to phonons, disregarding other sources of scattering. Therefore, these values should be seen only as an upper bound for the actual mobilities.

Chapter 5
Conclusions

In this work, we proposed and investigated structural and electronic properties of a novel two-dimensional material with formula $B_2N_2O_2$, which is regarded to arise from the oxidation of a hBN layer. For the proposal part, we employed the software USPEX along with VASP to predict the lowest-energy crystalline geometries for this chemical composition. The two best structures were found to be almost degenerate in energy and resulted in slabs presenting a similar geometry, with nitrogen sandwiched by boron, which, in turn, were bridged by oxygen. Remarkably, the nitrogen atoms presented bonds forming one-dimensional zigzag arrays in both parallel and perpendicular directions relative to the surface.

An in-depth theoretical characterization of these structures were performed using the *ab-initio* softwares SIESTA and VASP. Three structural calculations were conducted, namely, formation energy, phonon dispersion and molecular dynamics, and the results indicated a genuine stability of the structures. Besides the large negative formation energy, they are dynamically and thermally stable. An investigation on the electronic properties was then performed, in which we evaluated their band structure, projected density of states (PDOS), localized density of states (LDOS) and carrier mobilities. The considered structures were found to be wide-bandgap semiconductors with parabolic band edges within the HSE06 approximation for the exchange-correlation functional. From the PDOS and LDOS results, the conduction band edges were found to be defined by the nitrogen atoms, while the valence band edges were found to have contributions mainly split between nitrogen and oxygen. These results suggest that the nitrogen zigzag arrays play an important role on the electronic structure of the compounds. Indeed, we observe this tendency in the mobility calculations.

They were performed within the deformation potential framework and indicate that high electron and hole mobilities can be achieved. Many oxides suffer from low carrier mobilities due to the localized character of oxygen $2p$ orbitals. We associate the high mobilities achieved in this work to the nitrogen zigzag channels, which, as discussed, compose both the valence and conduction band edges and indicate that the potential mobility limitations of oxides can be overcome.

After performing a detailed characterization of the compounds, a potential simplified route to synthesize $B_2N_2O_2$ from an hBN layer and O_2 molecules was suggested. It involved a combination of oxygen functionalization, application of pressure and relaxation of the structures, which resulted in the perpendicular-zigzag geometry after going through some intermediate structures, including the third best structure found by USPEX. Lastly, we show that the perpendicular-zigzag structure may actually be extended to represent a family of oxide compounds. Indeed, we perform a brief characterization of a potential member of this family, $Al_2As_2O_2$, which is obtained by replacing B and N with Al and As in the perpendicular-zigzag geometry. This structure presents robust stability indicatives and similar electronic properties to the B-N counterpart and can be investigated in future works.

Bibliography

[1] Y. Liu, X. Duan, H.-J. Shin, S. Park, Y. Huang, and X. Duan, "Promises and prospects of two-dimensional transistors," *Nature*, vol. 591, p. 43–53, 2021.

[2] K. Khan, A. K. Tareen, M. Aslam, R. Wang, Y. Zhang, A. Mahmood, Z. Ouyang, H. Zhang, and Z. Guo, "Recent developments in emerging two-dimensional materials and their applications," *J. Mater. Chem. C*, vol. 8, pp. 387–440, 2020.

[3] T. R. Nayak, H. Andersen, V. S. Makam, C. Khaw, S. Bae, X. Xu, P.-L. R. Ee, J.-H. Ahn, B. H. Hong, G. Pastorin, and B. Özyilmaz, "Graphene for controlled and accelerated osteogenic differentiation of human mesenchymal stem cells," *ACS Nano*, vol. 5, no. 6, pp. 4670–4678, 2011. PMID: 21528849.

[4] A. Olabi, M. A. Abdelkareem, T. Wilberforce, and E. T. Sayed, "Application of graphene in energy storage device – a review," *Renewable and Sustainable Energy Reviews*, vol. 135, p. 110026, 2021.

[5] D. Cohen-Tanugi and J. C. Grossman, "Water desalination across nanoporous graphene," *Nano Letters*, vol. 12, no. 7, pp. 3602–3608, 2012. PMID: 22668008.

[6] H. Liu, J. Gao, and J. Zhao, "Silicene on substrates: A way to preserve or tune its electronic properties," *The Journal of Physical Chemistry C*, vol. 117, no. 20, pp. 10353–10359, 2013.

[7] W. Choi, N. Choudhary, G. H. Han, J. Park, D. Akinwande, and Y. H. Lee, "Recent development of two-dimensional transition metal dichalcogenides and their applications," *Materials Today*, vol. 20, no. 3, pp. 116–130, 2017.

[8] E. M. C. Fortunato, P. M. C. Barquinha, A. C. M. B. G. Pimentel, A. M. F. Gonçalves, A. J. S. Marques, R. F. P. Martins, and L. M. Pereira, "Wide-bandgap high-mobility ZnO thin-film transistors produced at room temperature," *Applied Physics Letters*, vol. 85, pp. 2541–2543, 09 2004.

[9] Y. Oshima and E. Ahmadi, "Progress and challenges in the development of ultra-wide bandgap semiconductor α-Ga2O3 toward realizing power device applications," *Applied Physics Letters*, vol. 121, 12 2022.

[10] R. Zheng, J. Lu, Y. Wang, Z. Chen, X. Zhang, X. Li, L. Liang, L. Qin, Y. Zeng, Y. Chen, and Y. Liu, "Understanding efficiency improvements of betavoltaic batteries based on 4H-SiC, GaN, and diamond," *Applied Physics Letters*, vol. 121, 09 2022.

[11] F. Roccaforte, P. Fiorenza, G. Greco, R. Lo Nigro, F. Giannazzo, F. Iucolano, and M. Saggio, "Emerging trends in wide band gap semiconductors (sic and gan) technology for power devices," *Microelectronic Engineering*, vol. 187-188, pp. 66–77, 2018.

[12] Y. Lu and J. H. Warner, "Synthesis and applications of wide bandgap 2d layered semiconductors reaching the green and blue wavelengths," *ACS Applied Electronic Materials*, vol. 2, no. 7, pp. 1777–1814, 2020.

[13] Y.-R. Chang, T. Nishimura, and K. Nagashio, "Thermodynamic perspective on the oxidation of layered materials and surface oxide amelioration in 2d devices," *ACS Applied Materials & Interfaces*, vol. 13, no. 36, pp. 43282–43289, 2021.

[14] A. C. R. Souza, M. J. S. Matos, and M. S. C. Mazzoni, "Oxidation-driven formation of precisely ordered antimonene nanoribbons," *Journal of Physics: Condensed Matter*, vol. 32, p. 165302, jan 2020.

[15] R. K. Singh, R. Kumar, and D. P. Singh, "Graphene oxide: strategies for synthesis, reduction and frontier applications," *RSC Adv.*, vol. 6, pp. 64993–65011, 2016.

[16] H. Jin, Y. Li, X. Li, Z. Shi, H. Xia, Z. Xu, and G. Qiao, "Functionalization of hexagonal boron nitride in large scale by a low-temperature oxidation route," *Materials Letters*, vol. 175, pp. 244–247, 2016.

[17] D. McIntyre, C. Manogue, and J. Tate, *Quantum Mechanics*. Pearson, 2016.

[18] A. Szabo and N. Ostlund, *Modern Quantum Chemistry: Introduction to Advanced Electronic Structure Theory*. Dover Books on Chemistry, Dover Publications, 1996.

[19] M. Born and R. Oppenheimer, "Zur quantentheorie der molekeln," *Annalen der Physik*, vol. 389, pp. 457 – 484, 03 1927.

[20] J. Kohanoff, *Electronic Structure Calculations for Solids and Molecules: Theory and Computational Methods*. Cambridge University Press, 2006.

[21] R. S. Mulliken, "Electronic structures of polyatomic molecules and valence. ii. general considerations," *Phys. Rev.*, vol. 41, pp. 49–71, Jul 1932.

[22] N. W. Ashcroft and N. D. Mermin, *Solid State Physics*. Holt-Saunders, 1976.

[23] P. Hohenberg and W. Kohn, "Inhomogeneous electron gas," *Phys. Rev.*, vol. 136, pp. B864–B871, Nov 1964.

[24] W. Kohn and L. J. Sham, "Self-consistent equations including exchange and correlation effects," *Phys. Rev.*, vol. 140, pp. A1133–A1138, Nov 1965.

[25] R. P. Feynman, "Forces in molecules," *Phys. Rev.*, vol. 56, pp. 340–343, Aug 1939.

[26] R. M. Martin, *Electronic Structure: Basic Theory and Practical Methods.* Cambridge University Press, 2020.

[27] J. P. Perdew and A. Zunger, "Self-interaction correction to density-functional approximations for many-electron systems," *Phys. Rev. B*, vol. 23, pp. 5048–5079, May 1981.

[28] D. M. Ceperley and B. J. Alder, "Ground state of the electron gas by a stochastic method," *Phys. Rev. Lett.*, vol. 45, pp. 566–569, Aug 1980.

[29] P. Taylor, P. Taylor, and O. Heinonen, *A Quantum Approach to Condensed Matter Physics.* Cambridge University Press, 2002.

[30] D. C. Langreth and M. J. Mehl, "Beyond the local-density approximation in calculations of ground-state electronic properties," *Phys. Rev. B*, vol. 28, pp. 1809–1834, Aug 1983.

[31] J. P. Perdew, K. Burke, and M. Ernzerhof, "Generalized gradient approximation made simple," *Phys. Rev. Lett.*, vol. 77, pp. 3865–3868, Oct 1996.

[32] A. D. Becke, "Density-functional exchange-energy approximation with correct asymptotic behavior," *Phys. Rev. A*, vol. 38, pp. 3098–3100, Sep 1988.

[33] J. P. Perdew and Y. Wang, "Accurate and simple analytic representation of the electron-gas correlation energy," *Phys. Rev. B*, vol. 45, pp. 13244–13249, Jun 1992.

[34] A. D. Becke, "A new mixing of hartree–fock and local density-functional theories," *The Journal of Chemical Physics*, vol. 98, no. 2, pp. 1372–1377, 1993.

[35] J. C. Phillips and L. Kleinman, "New method for calculating wave functions in crystals and molecules," *Phys. Rev.*, vol. 116, pp. 287–294, Oct 1959.

[36] E. Antončík, "Approximate formulation of the orthogonalized plane-wave method," *Journal of Physics and Chemistry of Solids*, vol. 10, no. 4, pp. 314–320, 1959.

[37] D. R. Hamann, M. Schlüter, and C. Chiang, "Norm-conserving pseudopotentials," *Phys. Rev. Lett.*, vol. 43, pp. 1494–1497, Nov 1979.

[38] N. Troullier and J. L. Martins, "Efficient pseudopotentials for plane-wave calculations," *Phys. Rev. B*, vol. 43, pp. 1993–2006, Jan 1991.

[39] J. M. Soler, E. Artacho, J. D. Gale, A. García, J. Junquera, P. Ordejón, and D. Sánchez-Portal, "The siesta method for ab initio order-n materials simulation," *Journal of Physics: Condensed Matter*, vol. 14, no. 11, p. 2745, 2002.

[40] G. Kresse and J. Furthmüller, "Efficient iterative schemes for ab initio total-energy calculations using a plane-wave basis set," *Phys. Rev. B*, vol. 54, pp. 11169–11186, Oct 1996.

[41] H. J. C. Berendsen, J. P. M. Postma, W. F. van Gunsteren, A. DiNola, and J. R. Haak, "Molecular dynamics with coupling to an external bath," *The Journal of Chemical Physics*, vol. 81, pp. 3684–3690, 10 1984.

[42] S. Nosé, "A unified formulation of the constant temperature molecular dynamics methods," *The Journal of Chemical Physics*, vol. 81, pp. 511–519, 07 1984.

[43] K. S. Novoselov, A. K. Geim, S. V. Morozov, D. Jiang, Y. Zhang, S. V. Dubonos, I. V. Grigorieva, and A. A. Firsov, "Electric field effect in atomically thin carbon films," *Science*, vol. 306, no. 5696, pp. 666–669, 2004.

[44] K. S. Novoselov, D. Jiang, F. Schedin, T. J. Booth, V. V. Khotkevich, S. V. Morozov, and A. K. Geim, "Two-dimensional atomic crystals," *Proceedings of the National Academy of Sciences*, vol. 102, no. 30, pp. 10451–10453, 2005.

[45] L. H. Li, J. Cervenka, K. Watanabe, T. Taniguchi, and Y. Chen, "Strong oxidation resistance of atomically thin boron nitride nanosheets," *ACS Nano*, vol. 8, no. 2, pp. 1457–1462, 2014. PMID: 24400990.

[46] A. Dideikin and A. Vul, "Graphene oxide and derivatives: The place in graphene family," *Frontiers in Physics*, vol. 6, 01 2019.

[47] L. H. Li, J. Cervenka, K. Watanabe, T. Taniguchi, and Y. Chen, "Strong oxidation resistance of atomically thin boron nitride nanosheets," *ACS Nano*, vol. 8, no. 2, pp. 1457–1462, 2014. PMID: 24400990.

[48] N. G. Doménech, Coogan, F. Purcell-Milton, M. L. Casasín García, A. S. Arjona, M. B. Cabré, A. Rafferty, K. McKelvey, P. Dunne, and Y. K. Gun'ko, "Partially oxidised boron nitride as a 2d nanomaterial for nanofiltration applications," *Nanoscale Adv.*, vol. 4, pp. 4895–4904, 2022.

[49] H. Jin, Y. Li, X. Li, Z. Shi, H. Xia, Z. Xu, and G. Qiao, "Functionalization of hexagonal boron nitride in large scale by a low-temperature oxidation route," *Materials Letters*, vol. 175, pp. 244–247, 2016.

[50] A. R. Oganov and C. W. Glass, "Crystal structure prediction using ab initio evolutionary techniques: Principles and applications," *The Journal of Chemical Physics*, vol. 124, no. 24, p. 244704, 2006.

[51] C. W. Glass, A. R. Oganov, and N. Hansen, "Uspex—evolutionary crystal structure prediction," *Computer Physics Communications*, vol. 175, no. 11, pp. 713–720, 2006.

[52] P. Jamdagni, A. Thakur, A. Kumar, P. K. Ahluwalia, and R. Pandey, "Two dimensional allotropes of arsenene with a wide range of high and anisotropic carrier mobility," *Phys. Chem. Chem. Phys.*, vol. 20, pp. 29939–29950, 2018.

[53] B. Zhang, H. Zhang, J. Lin, and X. Cheng, "First-principle study of seven allotropes of arsenene and antimonene: thermodynamic, electronic and optical properties," *Phys. Chem. Chem. Phys.*, vol. 20, pp. 30257–30266, 2018.

[54] N. Troullier and J. L. Martins, "Efficient pseudopotentials for plane-wave calculations," *Phys. Rev. B*, vol. 43, pp. 1993–2006, Jan 1991.

[55] L. Kleinman and D. M. Bylander, "Efficacious form for model pseudopotentials," *Phys. Rev. Lett.*, vol. 48, no. 20, pp. 1425–1428, 1982.

[56] J. P. Perdew, K. Burke, and M. Ernzerhof, "Generalized gradient approximation made simple," *Phys. Rev. Lett.*, vol. 77, no. 18, pp. 3865–3868, 1996.

[57] J. Heyd, G. E. Scuseria, and M. Ernzerhof, "Hybrid functionals based on a screened Coulomb potential," *The Journal of Chemical Physics*, vol. 118, pp. 8207–8215, 04 2003.

[58] J. Heyd, G. E. Scuseria, and M. Ernzerhof, "Erratum: "Hybrid functionals based on a screened Coulomb potential" [J. Chem. Phys. 118, 8207 (2003)]," *The Journal of Chemical Physics*, vol. 124, 06 2006.

[59] J. Shi, Z. Sheng, L. Zhu, X. Xu, Y. Gao, D. Tang, and K. H. L. Zhang, "The electronic structure of β-TeO2 as wide bandgap p-type oxide semiconductor," *Applied Physics Letters*, vol. 122, 03 2023. 101901.

[60] J. Bardeen and W. Shockley, "Deformation potentials and mobilities in non-polar crystals," *Phys. Rev.*, vol. 80, pp. 72–80, Oct 1950.

[61] J. Qiao, X. Kong, Z.-X. Hu, F. Yang, and W. Ji, "High-mobility transport anisotropy and linear dichroism in few-layer black phosphorus," *Nature communications*, vol. 5, no. 1, p. 4475, 2014.

[62] L. Peng, C. Wang, Q. Qian, C. Bi, S. Wang, and Y. Huang, "Complete separation of carriers in the ges/sns lateral heterostructure by uniaxial tensile strain," *ACS Applied Materials & Interfaces*, vol. 9, no. 46, pp. 40969–40977, 2017.

[63] Y. Cui, L. Peng, L. Sun, Q. Qian, and Y. Huang, "Two-dimensional few-layer group-iii metal monochalcogenides as effective photocatalysts for overall water splitting in the visible range," *J. Mater. Chem. A*, vol. 6, pp. 22768–22777, 2018.

[64] C. Zhang, R. Wang, H. Mishra, and Y. Liu, "Two-dimensional semiconductors with high intrinsic carrier mobility at room temperature," *Phys. Rev. Lett.*, vol. 130, p. 087001, Feb 2023.